J Neurophysiol 123: 259–276, 2020.
First published November 20, 2019; doi:10.1152/jn.00883.2018.

RESEARCH ARTICLE | *Advances in Vestibular Research: A Tribute to Bernard Cohen, MD*

Binocular 3D otolith-ocular reflexes: responses of chinchillas to prosthetic electrical stimulation targeting the utricle and saccule

Kristin N. Hageman,[1] Margaret R. Chow,[1] Dale Roberts,[2] Peter J. Boutros,[1] Angela Tooker,[3] Kye Lee,[3] Sarah Felix,[3] Satinderpall S. Pannu,[3] Razi Haque,[3] and Charles C. Della Santina[1,2]
[1]*Department of Biomedical Engineering, Johns Hopkins School of Medicine, Baltimore, Maryland;* [2]*Department of Otolaryngology–Head and Neck Surgery, Johns Hopkins School of Medicine, Baltimore, Maryland; and* [3]*Lawrence Livermore National Laboratory, Livermore, California*

Submitted 31 December 2018; accepted in final form 9 November 2019

Hageman KN, Chow MR, Roberts D, Boutros PJ, Tooker A, Lee K, Felix S, Pannu SS, Haque R, Della Santina CC. Binocular 3D otolith-ocular reflexes: responses of chinchillas to prosthetic electrical stimulation targeting the utricle and saccule. *J Neurophysiol* 123: 259–276, 2020. First published November 20, 2019; doi: 10.1152/jn.00883.2018.—From animal experiments by Cohen and Suzuki et al. in the 1960s to the first-in-human clinical trials now in progress, prosthetic electrical stimulation targeting semicircular canal branches of the vestibular nerve has proven effective at driving directionally appropriate vestibulo-ocular reflex eye movements, postural responses, and perception. That work was considerably facilitated by the fact that all hair cells and primary afferent neurons in each canal have the same directional sensitivity to head rotation, the three canals' ampullary nerves are geometrically distinct from one another, and electrically evoked three-dimensional (3D) canal-ocular reflex responses approximate a simple vector sum of linearly independent components representing relative excitation of each of the three canals. In contrast, selective prosthetic stimulation of the utricle and saccule has been difficult to achieve, because hair cells and afferents with many different directional sensitivities are densely packed in those endorgans and the relationship between 3D otolith-ocular reflex responses and the natural and/or prosthetic stimuli that elicit them is more complex. As a result, controversy exists regarding whether selective, controllable stimulation of electrically evoked otolith-ocular reflexes (eeOOR) is possible. Using micromachined, planar arrays of electrodes implanted in the labyrinth, we quantified 3D, binocular eeOOR responses to prosthetic electrical stimulation targeting the utricle, saccule, and semicircular canals of alert chinchillas. Stimuli delivered via near-bipolar electrode pairs near the maculae elicited sustained ocular countertilt responses that grew reliably with pulse rate and pulse amplitude, varied in direction according to which stimulating electrode was employed, and exhibited temporal dynamics consistent with responses expected for isolated macular stimulation.

NEW & NOTEWORTHY As the second in a pair of papers on Binocular 3D Otolith-Ocular Reflexes, this paper describes new planar electrode arrays and vestibular prosthesis architecture designed to target the three semicircular canals and the utricle and saccule. With this technological advancement, electrically evoked otolith-ocular reflexes due to stimulation via utricle- and saccule-targeted electrodes were recorded in chinchillas. Results demonstrate advances toward achieving selective stimulation of the utricle and saccule.

otolith-ocular reflex; saccule; utricle; vestibular; vestibular prosthesis

INTRODUCTION

The mammalian inner ear's vestibular labyrinth comprises two types of motion sensors, three semicircular canals and two otolith (otoconial) end organs, that together provide sensation of head movement and orientation to drive reflexes to maintain stable vision and posture. The three mutually orthogonal, fluid-filled semicircular canals in one ear form coplanar pairs with the canals in the opposite ear, with each pair encoding one of three components of three-dimensional (3D) rotational head velocity: left-anterior/right-posterior (LARP), right-anterior/left-posterior (RALP), and left-horizontal/right-horizontal (LHRH). During a head rotation about the axis of a given canal, the stereocilia of hair cells in that canal's ampulla deflect due to inertial loading by the fluid in the canal. This deflection ultimately drives changes in firing rates of the canal's afferent neurons. Hair cells in one canal are all oriented in the same direction, so an excitatory head rotation about that canal's axis excites every hair cell and afferent fiber in that canal (although for some afferents that excitation is subthreshold) while at the same time inhibiting every hair cell and afferent fiber in the coplanar canal. The difference between activity from the two canals effectively drives that plane's component of the eye-stabilizing angular vestibulo-ocular reflex (aVOR), resulting in eye rotational velocity approximately equal, opposite, and simultaneous with head rotation (Carey and Della Santina 2005; Goldberg et al. 2012).

The two otolith endorgans, the utricle and saccule, encode gravitoinertial acceleration (GIA), which comprise dynamic, relatively brief accelerations due to head translation [driving the translational VOR (tVOR)] and relatively long duration changes in the gravitational acceleration vector during head tilts (driving ocular counterroll and counterpitch responses) (Cohen et al. 2001). For brevity, the term otolith-ocular reflex (OOR) will be used here to denote both the tVOR and ocular

Address for reprint requests and other correspondence: C. Della Santina, Dept of Biomedical Engineering and Dept of Otolaryngology-Head and Neck Surgery, Johns Hopkins School of Medicine, Baltimore, MD 21205 (e-mail: cds@jhmi.edu).

countertilt and countertilt will be used to denote both counterroll and counterpitch. Hair cells of the utricle and saccule are located on each sensor's macula and are sensitive to shear forces imparted on hair cell stereocilia by an overlying mass of calcium carbonate crystals in a gelatinous medium called the otoconial membrane. During linear accelerations or changes in the GIA during static head tilt, loading by this mass causes displacement of the otoconial membrane, deflecting stereocilia and driving changes in firing rates of the macular nerve afferents, which subsequently drives OOR eye movements. The utricular macula lies approximately in the horizontal canal plane, sensing linear forces along any translation axis in that two-dimensional (2D) plane. The saccular macula is approximately oriented in a parasagittal plane, contributing the vertical dimension of translational acceleration. The hair cells on the utricle and saccule have nonuniform polarities; thus head translation along one direction normally causes a complex pattern of excitation of some hair cells and inhibition of others within the same end organ (Carey and Della Santina 2005; Goldberg et al. 2012). Each otolith afferent nerve fiber has a vector of maximum sensitivity to head movement. Head movements parallel to this vector produce the greatest change in afferent fiber firing rate; translations along other directions act according to cosine dependence between the motion axis and the fiber's maximum sensitivity vector (Angelaki 1991, 1992; Goldberg et al. 1984, 1990a, 1990b).

Loss of normal canal and otolith end organ sensation can result from a variety of insults to vestibular hair cells, including ototoxic injury, infection, autoimmune disease, ischemia, trauma, Ménière's disease, and effects of genetic abnormalities. Bilateral loss results in significant disability due to the failure of eye-, head-, and body-stabilizing reflexes; disruption of vestibulo-autonomic regulation; altered spatial perception; and cognitive fogging due to the expenditure of conscious effort necessitated by failure of normally subconscious, automatic reflexes (Carey and Della Santina 2005; Yates and Bronstein 2005; Yates and Miller 1994; Zhu et al. 2007). Humans disabled by bilateral vestibular hypofunction experience blurry vision, oscillopsia (illusory movement of the visual field), unsteady gait, and overall poor quality of life (Priesol et al. 2014; Strupp et al. 2017; Sun et al. 2014; Valko et al. 2012; Ward et al. 2013). Rehabilitation exercises can help affected individuals compensate using visual and proprioceptive cues (Krebs et al. 1993; Whitney and Rossi 2000), and at least one clinical trial seeking to generate new hair cells is currently underway (ClinicalTrials.gov 2018a); however, there is currently no cure that restores canal and otolith end organ function after severe loss due to hair cell injury.

Efforts to restore canal sensation of head rotation using a vestibular implant (a head-mounted prosthetic electrical stimulator analogous to a cochlear implant) started with work in guinea pigs by Gong and Merfeld (2000), continued through numerous studies in chinchillas and nonhuman primates (e.g., Chiang et al. 2011; Dai et al. 2011a, 2011b, 2011c, 2013; Davidovics et al. 2011, 2012, 2013; Della Santina et al. 2007; Fridman et al. 2010; Gong et al. 2008; Gong and Merfeld 2000; Lewis et al. 2002–2003, 2010, 2011, 2013a, 2013b; Merfeld et al. 2006, 2007; Mitchell et al. 2013; Nie et al. 2013; Phillips et al. 2016, 2018; Sun et al. 2015; Valentin et al. 2013), and have led to three actively recruiting first-in-human clinical trials (Boutros et al. 2018; ClinicalTrials.gov 2018b; Golub et al. 2014; Guyot and Perez Fornos 2019; Phillips et al. 2015; Wall et al. 2007). Those canal stimulation efforts built on three foundations. First, extensive literature describes aVOR responses of normal animals to natural head rotation stimuli (reviewed in Leigh and Zee 2006). Second, the selective prosthetic electrical stimulation of semicircular canal ampullary nerves had already been clearly established in a classic 1960s series of experiments by Cohen, Suzuki, and colleagues, who showed in multiple species that electrical stimulation via wires implanted in one or more semicircular canal ampullae can drive binocular, conjugate aVOR eye movements that rotate about an axis that aligns with a weighted vector sum of the three canals' anatomic axes. Third, because the aVOR eye movement responses driven by canal stimulation can be well approximated by a one-to-one linear vector mapping from relative canal stimulation to eye movement axis, the inverse of that 3D linear algebraic relationship can be used to estimate the relative degree to which a stimulating electrode's current is exciting each semicircular canal's ampullary nerve (Fridman et al. 2010). Insight provided by this simple input-output relationship facilitated optimization of electrode designs and stimulus parameters (Fridman and Della Santina 2012) because it allowed investigators to assay performance of the electrode-nerve stimulation interface indirectly via 3D video- or scleral coil oculography.

In contrast to the comparatively well-paved path facilitating prosthetic canal stimulation research, prosthetic stimulation of the utricle and saccule presents a more challenging foray into less well explored territory. Normal OORs have been characterized in multiple species, starting with 19th century studies in birds (Breuer 1891) and extending to more recent studies in rodents, cats and primates (Angelaki 1998; Angelaki et al. 2002; Angelaki and Hess 1996a, 1996b; Baarsma and Collewijn 1975; Cohen et al. 2001; Fluur and Mellström 1970a, 1970b; Gianna et al. 1997; Maruta et al. 2001; Zee and Hain 1992), as reviewed in Leigh and Zee (2006); however, they are less well described than the aVOR. Compared with aVOR responses, OOR responses are typically smaller, often near the noise floor of oculographic recording systems, and more species dependent. Moreover, OORs are not as readily described by a simple, reversible 3D mapping from head movement to eye movement like the one that follows from seminal studies by Ewald, Tullio, Cohen, Suzuki, and others (reviewed in Carey and Della Santina 2005; Leigh and Zee 2006), because they are often disconjugate (so the responses of 2 eyes comprise 6-dimensional data) and the GIA stimulus encoded by the utricle and saccule comprises not only the three components due to head translational acceleration but also three overlapping components due to head tilt with respect to gravity (making the stimulus 6-dimensional). Although a normal subject might disambiguate this tilt-translation confusion by integrating canal and otolith inputs over time (Angelaki et al. 2004) or by considering stimulus timing in the context of prior experience (Paige and Seidman 1999), an experimentalist seeking to interpret oculographic data in terms of the head translation and tilt stimuli that would normally generate the observed responses faces a mathematically indeterminate problem.

Further obscuring the path to effective prosthetic stimulation of the utricle and saccule are the dense packing of hair cells and afferent fibers with different directional sensitivities in each

macula and the fact that the few publications describing attempts to generate electrically evoked OORs yielded conflicting results. From early studies in birds (Breuer 1891), initial findings in cats (Suzuki et al. 1969), and results from the studies of Goto et al. (2003, 2004) in cats, utricle and saccule stimulation generally elicited a limited range of eye movements often in one or two directions, likely due to current spread. Acute utricular and saccular stimulation in spinalized and decerebrate cats by Fluur and Mellström (1970a, 1970b, 1971) resulted in responses more suggestive of selective stimulation, including eye movements that reportedly varied with location of stimulating electrode on the macula. However, a subsequent effort by Curthoys (1987) to replicate those experiments yielded results inconsistent with those of Fluur and Mellström (1970a, 1970b, 1971).

Discrepancies among the limited number of studies that have attempted selective electrical stimulation of the utricle or saccule suggest a need for further investigation to determine the feasibility of spatially selective (and prosthetically effective) utricle and saccule stimulation. Using results of the companion study (Hageman et al. 2020) characterizing 3D binocular OOR responses to tilt and translation in normal chinchillas as a guide to the range and type of eye movements prosthetic utricular and/or saccular stimulation should ultimately achieve, we evaluated the feasibility of selectively stimulating different subsections of the utricle and saccule using high-density microelectrode arrays fabricated using techniques analogous to arrays employed in retinal implants used in humans (da Cruz et al. 2016).

METHODS

Electrode design and fabrication. Due to the nonuniform polarity of hair cells in the utricle and saccule, a more complex electrode array is needed to provide stimulation contacts across the maculae compared with the canal electrode arrays we have used for prior studies (Chiang et al. 2011; Della Santina et al. 2007). A new electrode array was designed using a 3D anatomical chinchilla model reconstructed from microcomputed tomography (microCT) scans described previously in Hayden et al. (2011) shown in Fig. 1*A*. We identified a surgical approach to target the utricle, saccule, and all three canals, and then, we designed the electrode array to fit the geometry of the chinchilla labyrinth based on measurements taken from this 3D model. The design goal was to place 2D arrays of electrode contacts near the utricle and saccule maculae (Fig. 1*B*) and a linear array of electrode contacts in each canal's ampulla.

Based on design constraints and anatomical dimensions, the electrode array has 13 electrode contacts for the utricle and 13 for the saccule with 8 for each of the canals, giving a total of 50 electrode contacts, shown in Fig. 1*C*. Each electrode contact is 101 μm in diameter of activated iridium oxide film (AIROF). AIROF was used due to its significant increase in the allowable safe charge per area (1,200 μC/cm^2) compared with bare platinum electrodes (24 μC/cm^2) (Robblee and Rose 1990). These electrodes can safely use up to 400 μA at 200 μs/phase (or any pulse amplitude and pulse width to give an equivalent μA $\times$ μs/phase) while staying under this safety limit. Electrode numbers are shown in Fig. 2.

Electrode arrays were fabricated using a two-layer metal, multicontact, polymer electrodes design, following standard MEMS fabrication techniques, previously described in Tooker et al. (2012) and shown in Fig. 3. For a brief summary, the processing steps begin with a 5-μm deposition of a polyimide layer (Fig. 3*A*) followed by deposition and patterning of trace metal 1 (Ti/Au/Ti, shown in Fig. 3*B*). A second layer of polyimide (2 μm) is deposited atop the trace metal (Fig. 3*C*) before O_2 plasma etching for interconnection vias (Fig. 3*D*). A second layer of Ti/Au/Ti trace metal is deposited and patterns (Fig. 3*E*) followed by the deposition and patterning of the electrode metal (Ir, Fig. 3*F*). A final layer of polyimide is deposited (5 μm, Fig. 3*G*) before electrode vias are etched using O_2 plasma (Fig. 3*H*). Finally, the device outline is etched using O_2 plasma (Fig. 3*I*). The iridium electrode contacts were activated using biphasic potential pulses in phosphate-buffered saline, forming the AIROF. An average

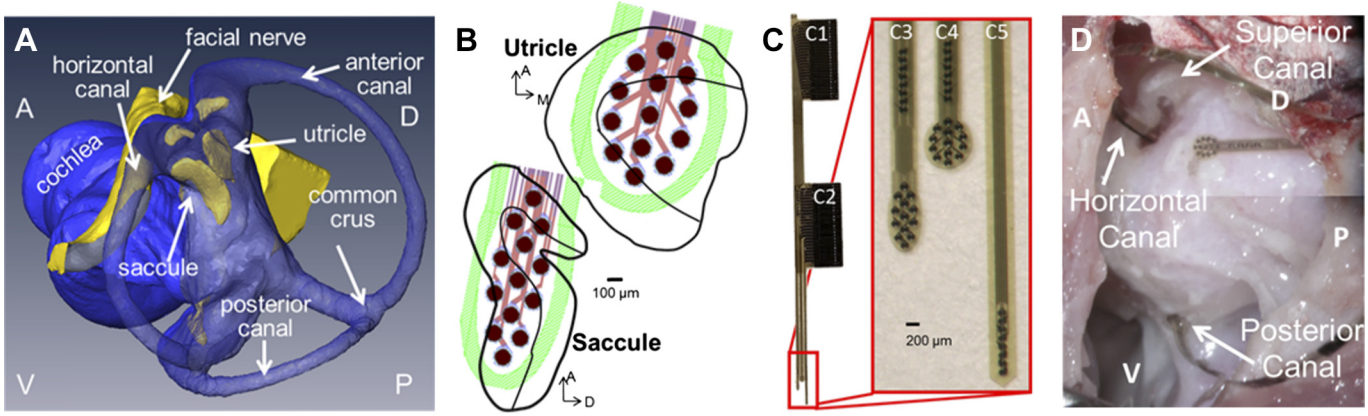

Fig. 1. Electrode design for a vestibular implant that stimulates all 5 vestibular end organs. *A*: 3-dimensional (3D) reconstruction of chinchilla microcomputed tomograhy and microMRI scans (Hayden et al. 2011) was used to design new electrode arrays to target the utricle and saccule (blue indicates the lumen and yellow the neural epithelium). A, anterior; P, posterior; D, dorsal; H, horizontal. *B*: the electrode array was designed to have as many contacts on the utricle and saccule while still maintaining safe charge injection. With these constraints, in addition to those from the fabrication process, an array of 13 activated iridium oxide film (AIROF) electrodes for the utricle and 13 for the saccule (outlines of end organs adapted from Desai et al. 2005) were designed to lay on the macular surface of each end organ. *C*: the polyimide/gold/AIROF array has 2 large connectors (*C1* and *C2*) through which a printed circuit board can connect to the array's 50 electrodes on 3 different shanks. The 1st shank (C3) has 8 contacts to target the horizontal semicircular canal and the array of 13 for the saccule, the next shank (*C4*) has 8 contacts for the superior canal with 13 for the utricle, and the final shank (*C5*) has 8 electrodes for the posterior canal. *D*: view from postero-supero-lateral through a surgical microscope during electrode implantation. The surgical approach through the bulla of the chinchilla provides access to all 3 canal ampullae. A small hole was made in or near each ampulla, and the electrode array shank with 8 posterior canal electrodes was inserted to a predetermined depth based on the 3D anatomical model shown in *A*. The horizontal canal + saccule and the anterior canal + utricle shanks are inserted through openings made near each canal's ampulla. Placement of electrodes targeting utricle and saccule relies on canal bone landmarks, the trajectory of insertion and electrode array geometry.

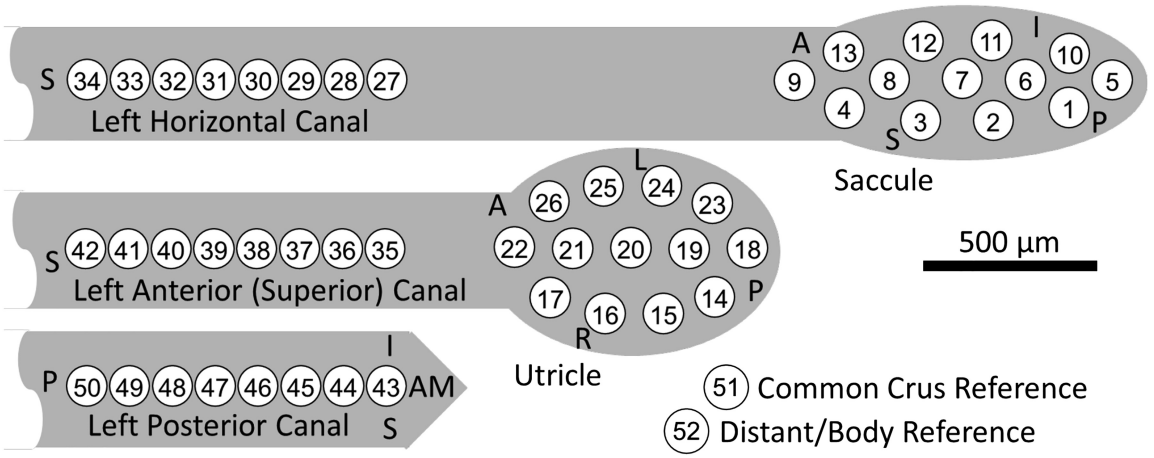

Fig. 2. Polyimide electrode array contact numbering scheme. *Electrodes 1–13* are intended for the saccule, *electrodes 14–26* the utricle, *electrodes 27–34* for the left horizontal semicircular canal, *electrodes 35–42* for the left superior canal, and *electrodes 43–50* for the left posterior canal. Teflon-coated, 75-μm diameter Pt/Ir wire reference *electrodes 51* (the "common crus reference," inserted in the common crus) and *52* (the "distant/body reference," embedded in neck musculature) were stripped ~1 and ~10 mm, respectively. Orientation directions shown (S, superior; A, anterior; I, inferior; L, left; R, right; and AM, anteromedial) signify the approximate intended orientation for surgical implantation in left labyrinth.

impedance of 12.2 ± 3.1 kOhm at 10 kHz was recorded in one representative array, as reported in Hageman et al. (2016a).

Each electrode array was connected to a small custom-printed circuit board (PCB) and epoxied in place before gas sterilization for implantation. Two Pt/Ir wires (Cooner Wire, AS 169-40) were also connected to the PCB for a common crus electrode and a distant electrode in muscle. The PCB routes each of the 50 electrodes, and the distant and common crus electrodes, to two connectors that act as a percutaneous connection for the stimulation circuitry.

Circuit design: hardware, firmware, and software. To accommodate the new electrode array with an increased number of electrodes, the prosthesis architecture we have previously employed for animal studies of canal stimulation was updated as shown in Fig. 4. Although this architecture is similar to that of previous generations (Chiang et al. 2011; Della Santina et al. 2007), changes were required to extend the prosthesis to include utricle, saccule and canal stimulation, briefly discussed in Hageman et al. (2016a). The system architecture has four main blocks, *1*) custom C# software for wireless programming of the prosthesis; *2*) a microcontroller, *3*) a custom application specific integrated circuit (ASIC), which provides stimulation management (described in full in Hageman et al. 2016b); and *4*) a crosspoint switch to select which of the 52 electrodes to use. The system runs off of a 3.7-V rechargeable Li-Ion battery, which is regulated to 3.3 V for the microcontroller and uses a step-up converter to reach 5 and 12 V, which are both needed for the custom ASIC.

The C# software provides a streamlined graphical user interface (GUI) to wirelessly program the prosthesis using Bluetooth protocol. The software allows for straightforward connection between the microcontroller, ASIC, and crosspoint switch to program the stimulating and reference electrodes (blue arrows in Fig. 4). Multiple stimulation paradigms are possible with this software; however, "virtual sinusoidal rotation or translation" and "virtual static tilt" (changes in pulse rate to encode a head movement while the animal is held still and in complete darkness) were the primary focus for this experiment. The GUI software sends all necessary parameters to the microcontroller to complete each stimulation set and also communicates with the software used for the coil system to synchronize stimulation and eye movement recording files (yellow arrows in Fig. 4).

A microcontroller (MSP430F5338; Texas Instruments) communicates with the C# GUI to run each experimental paradigm, manage

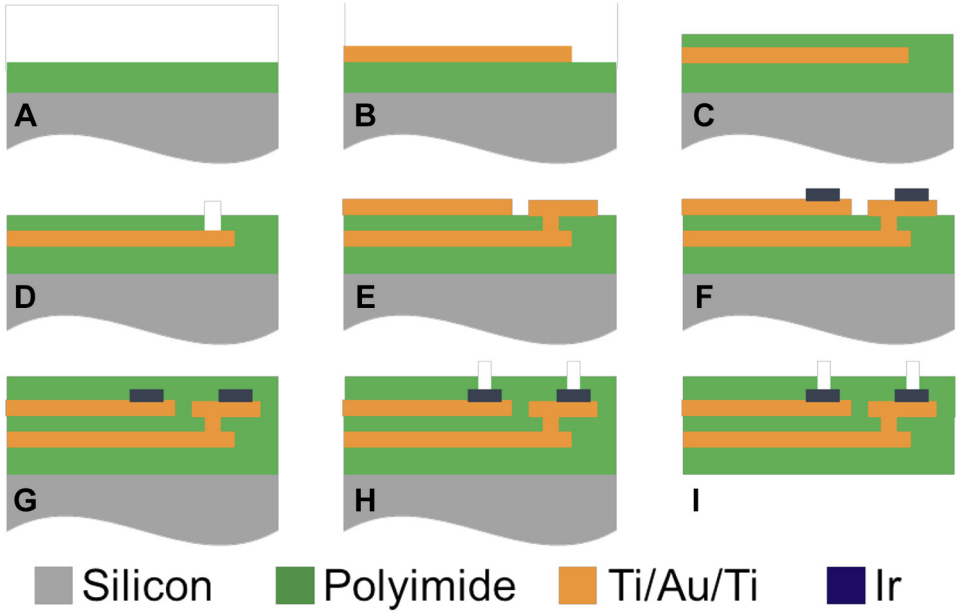

Fig. 3. Cross-sectional view of the microfabrication process for electrode arrays. *A*: deposition of 5-μm Polyimide 1 layer (green) atop a silicon wafer substrate (gray). *B*: deposition and patterning of trace metal 1 (Ti/Au/Ti). *C*: polyimide 2 deposition (2 μm). *D*: interconnection via etching (achieve using O_2 plasma). *E*: deposition and patterning of trace metal 2 (Ti/Au/Ti). *F*: deposition and patterning of Ir electrode metal. *G*: polyimide 3 deposition (5 μm). *H*: electrode via etching. *I*: device outline etching. Images are not drawn to scale and adapted with permission from Tooker et al. 2012).

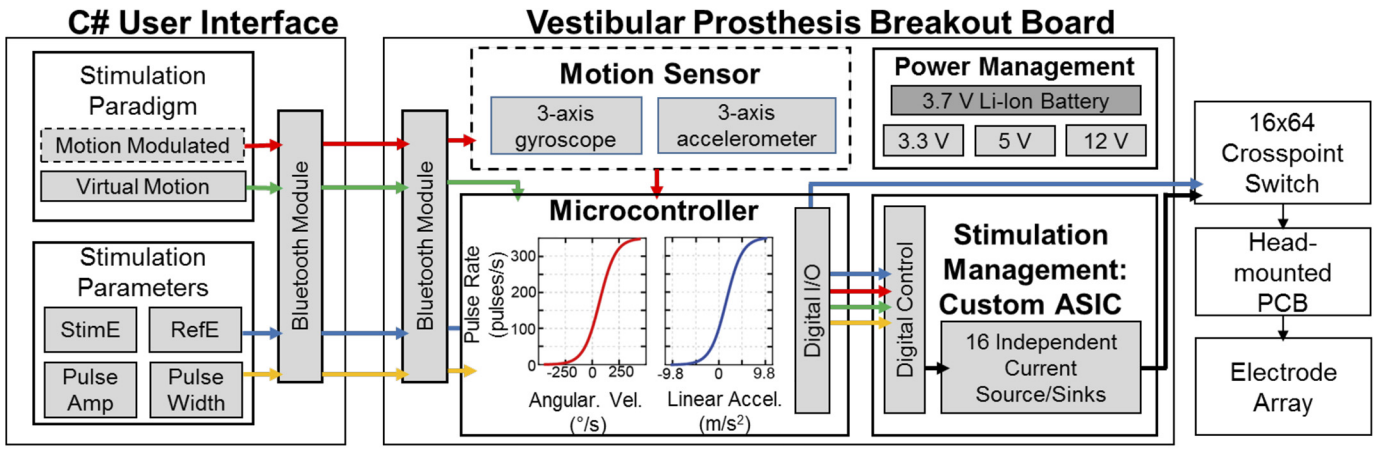

Fig. 4. New multichannel vestibular prosthesis system design, created to interface with the new electrode arrays to stimulate the utricle and saccule. Although similar to the previous system (Chiang et al. 2011; Della Santina et al. 2007), additions to the software, hardware, and firmware were required to encode and stimulate translations and static tilts. A custom C# graphical user interface (GUI) was created to program the prosthesis via Bluetooth. The GUI programs all stimulation parameters, such as stimulating electrode, reference electrode, and pulse amplitude and width. Additionally, the GUI controls the stimulation paradigm instructions sent to the prosthesis microcontroller set the pulse rate modulation. Although motion triggered pulse frequency modulation was not used for experiments detailed in this study, the system architecture was created to easily integrate a motion sensor in the future. All virtual modulation paradigms change the pulse rate in order to encode a virtual movement while the animal is kept still. The microcontroller commands the passive application specific integrated circuit neural interface (ASIC-NI) (Hageman et al. 2016b). The ASIC-NI's 16 output channels can be connected to any of the 52 electrodes (50 on the polyimide array, plus two additional distant electrodes in common crus and muscle) via a crosspoint switch that connects to the animal's percutaneous electrode connector. PCB, printed circuit board.

pulse timing, and program the ASIC and crosspoint switch appropriately for each pulse that is delivered. Although all of the data collected for this paper had a "virtual" head movement stimulus instead of motion sensor driven changes in pulse rate, the prosthesis was designed to easily integrate a 6 degree-of-freedom motion sensor (MPU9250; Invensense) for experiments in the future (dashed boxes and red arrows in Fig. 4). The microcontroller drives the passive ASIC chip, to program the pulse amplitude, polarity, and the global enable to begin stimulation on the stimulating and reference electrodes. The microcontroller also sends a digital pulse to the coil system to be saved with all eye movement data to directly correlate eye movements with the timing of the pulsatile stimulation.

For detailed specifications on the custom ASIC, see Hageman et al. (2016b). In brief, the ASIC contains 16 individual source/sink pairs so that each channel can be programmed as a stimulating or reference electrode. The ASIC operates at 5 V, with a 12-V compliance. With the impedance of these electrodes, this compliance voltage offers pulses up to ~1 mA which is beyond what is used based on safe charge injection rules. Each channel output has a 1-μF DC-coupling capacitor.

The crosspoint switch board contains four 16 $\times$ 16 multiplexers to give an overall 16 $\times$ 64 multiplexer. This allows any of the 16 ASIC output channels to be connected to any of the 50 electrode contacts or 2 reference electrodes. The crosspoint switch uses a straight-forward TTL programming scheme, which is commanded by the microcontroller firmware and C# GUI. The crosspoint output is connected directly to the head-mounted PCB that provides a percutaneous connection to the 52 implanted electrodes.

Surgical methods. All experiments were performed using three normal adult chinchillas (*Chinchilla lanigera*, animals *Ch128*, *Ch132*, and *Ch133*). Surgical procedures were conducted in accordance with a protocol approved by the Johns Hopkins Animal Care and Use Committee, which is accredited by the Association for the Assessment and Accreditation of Laboratory Animal Care International and consistent with European Community Directive 86/609/EEC. After the surgical implant of scleral eye coils, described in detail in the companion paper (Hageman et al. 2020) and following the completion of normal data collection, a second surgery to implant the electrode array was completed.

Under general anesthesia (isoflurane, 1.5–5%), an electrode was implanted in the animal's left ear using an approach through the posterior bulla as shown in Fig. 1*D*. To place the posterior canal electrodes, a small hole was drilled into the posterior canal and the electrode shank was threaded into the canal until the contacts reached approximately to the posterior ampulla (this distance was measured with the 3D chinchilla model and marked on the electrode array preoperatively). Two small openings were drilled into the horizontal and anterior canal ampullae. The two holes were connected to allow for easier manipulation of the electrode shanks during insertion. Since the utricle and saccule targets cannot be seen from the surgical view, we relied on the predetermined geometry of the electrode array for guidance to the utricle and saccule. While a direct insertion into the labyrinth may achieve more accurate placement, we aimed to minimize the number of electrode shanks that needed to be inserted to decrease the risk of displacement of electrodes. Additionally, in chinchillas and rhesus, the semicircular canals circumscribe a nearly spherical portion of cerebellum, the parafloccculus, which makes a transbola approach more risky and difficult. Each electrode shank (saccule + LH canal, and utricle + LA canal) was carefully inserted into the drilled holes with the electrode contacts on the electrode array's anterior surface. Once the electrodes targeting the canals reached the ampulla, we used fascia to hold the electrode shank in place and then cemented the array into place using dental acrylic. One Pt/Ir reference wire was placed in the common crus, and a second distant reference wire was placed in the muscle. The small PCB used to connect to the electrode and provide the percutaneous connection for experiments was cemented to the head cap using dental acrylic. The animal recovered for 5–7 days before we proceeded with stimulation experiments.

Eye movement recording. 3D binocular eye movements were recorded using a custom magnetic scleral coil system adapted from the system first described by Robinson (1963). All eye movements are reported in head coordinate frame following the right-hand rule, where $+X$ is nasal, $+Y$ is out the left ear, and $+Z$ is superior. In brief, our custom system, described in the companion paper (Hageman et al. 2020) uses alternating magnetic fields operating at three different frequencies to induce a voltage in implanted scleral coils. The induced scleral coil voltage from each of the four implanted scleral coils is

sampled at 25 MHz and demodulated in the digital domain to determine the *X*, *Y*, and *Z* orientation of each scleral coil. Demodulated data were averaged over 50 ksamples to acquire a 1-kHz signal on a PC using custom program developed in C. This new system achieves a peak-to-peak noise floor $<0.024°$.

During experiments, the animal was head-fixed in a plastic cylindrical enclosure with the head centered in the middle of the coil frame. Before the stimulation paradigm began, we collected the gains of the coil system and any offsets of implanted scleral coils. The gains were measured by facing a nonimplanted scleral coil directly into each of the three magnetic fields to record the relative maximum voltage of each field. We connected each of the four implanted scleral coils to the coil system and quantified the offsets. All experiments were completed in total darkness to avoid visual suppression of the VOR.

Experimental methods. All experiments were completed in darkness, to avoid visual suppression of the VOR, with the animal's head fixed in the center of the coil system frame with the head tilted down ~50° to align the horizontal canals with Earth horizontal (Hullar and Williams 2006). The animals were not treated with gentamicin to ablate the hair cell stereocilia and cause vestibular loss, instead, "virtual movements" were created using changes in stimulation rate while the animal's head was kept still. All pulses were 100 μs/phase with a 50-μs interphase gap. During the first experiment for each animal, current thresholds were determined by turning on stimulation for each electrode and slowly increasing to a maximum of 200 μA/phase. We kept 200 μA as our maximum to provide a large safety buffer during the first experiments of this kind; this limit is well within the "safe charge injection" range for an AIROF electrode of this diameter. If any sign of facial nerve activation was seen before the 200-μA level was reached, that value was set as the maximum, and a value of 80% of maximum was used, otherwise 200 μA was used as the maximum. Electrode contacts were numbered as shown in Fig. 2. High-resolution microCT imaging to determine electrode location could not be completed on live animals and was therefore necessarily deferred until postmortem, after completion of all experiments. Therefore, *saccule stimulation* refers here to stimulation via electrodes intended to target the saccule (*electrode contacts 1–13*), *utricle stimulation* refers to stimulation via electrodes intended to target the utricle (*electrode contacts 14–26*), and *canal stimulation* refers to stimulation via electrodes intended to target the three canals (*electrode contacts 27–50*).

At the beginning of each experiment session, 10 cycles of a virtual rotation were delivered to each of the 24 electrodes targeting the semicircular canals (SCCs) using the common crus reference to track any changes in electrically evoked VOR over time. The virtual rotation (electrical stimulation to encode a head movement delivered while the animal is kept still) used a sinusoidal modulation of pulse rate of a pulse train of biphasic charge-balance constant-current pulses delivered via an electrode in each canal ampulla. The changes in pulse rate to encode this sinusoidal rotational velocity were determined based on the changes in firing rates acquired from neural recordings during rotations (Hullar et al. 2005). The pulse rate changes were encoded using a sigmoidal map (to map pulse rate to angular velocity) with the following parameters: baseline rate of 100 pulses/s (pps), maximum of 350 pps, minimum of 0 pps, and compression factor of 3 mapped to $\pm$ 500°/s angular velocity. Each virtual rotation was a 1-Hz sinusoid with peak 100°/s. The sigmoidal map is shown in the block diagram in Fig. 4.

A step change in pulse rate was delivered via every utricle and saccule electrode using the common crus, distant, and a subset of near-bipolar, reference electrodes. Each 40-s pulse train used a step change in pulse rate from zero to the pulse train rate (ranging from 50 to 300 pps). The pulse train was on for 40 s; stimulation stopped to indicate the end of the virtual static tilt/pulse train.

Data were acquired over four, nine, and six test sessions in animals *Ch128*, *Ch132*, and *Ch133*, respectively. Each session lasted ~3 h. Animals were euthanized after completion of VOR data acquisition so that microCT imaging could be performed to assay electrode location.

Eye movement analysis. We developed custom data analysis software package in Matlab (MathWorks, Natick, MA) that employs methods of rotational kinematics detailed in (Haslwanter 1995; Migliaccio and Todd 1999). In brief, for each of the four scleral coils, the coil system demodulated the coil voltage into its three dominant frequency components, which represented the *X*, *Y*, and *Z* components of the coil's axis with respect to the field coil frame. Data from the two scleral coils per eye were first mathematically orthogonalized to account for variability in placement on the scleral surface. For virtual rotations, the orthogonalized data were converted to a rotation vector and then to angular eye velocity vectors. Each binocular component of angular eye velocity (R_X, R_Y, R_Z, L_X, L_Y, and L_Z) was fit with a single frequency discrete Fourier transform at the frequency of the virtual rotation. The axis of eye velocity was determined based on the value of the eye velocity at peak positive stimulation rate. The average rotation vector during virtual tilt was calculated during the last five second of the stimulus and used to represent the final ocular countertilt position.

Imaging of electrode. We assayed electrode location using a SuperArgus CT scanner (Sedecal, Spain) microCT scan. Scan parameters were set to acquire 1,080 projections at high resolution, with 1×1 binning, 65 kV, 100 μA, 200-ms exposure, resulting in 32-μm isotropic voxel size and the capability to visualize the implanted electrodes with minimized metal artifact. Due to equipment constraints, all scans were completed postmortem on specimens trimmed to fit the scanner's narrow field of view; therefore, all physiologic data collection and analysis were blinded in that they were performed before knowing the exact location of the electrode arrays. MicroCT segmentation was completed using Amira (FEI Visualization Sciences Group, Bordeaux, France). Figure 5 shows the segmented CTs for the three chinchillas.

Back-projecting from eye movements to equivalent tilt axis using ocular countertilt responses of normal animals. Eye movements elicited by static tilts were the focus of this feasibility study, because in chinchillas they are larger than responses elicited by translations (Hageman et al. 2020). Our goal was to elicit ocular countertilt responses to prosthetic stimuli that span the space of possible OOR responses that normal chinchillas exhibit during head tilts about a wide variety of Earth-horizontal axes. To accomplish this goal, one must be able to selectively stimulate different parts of the utricular and/or saccular macular or nerves with different electrodes. Unable to directly observe current flow or patterns of hair cell and neuronal activation, we could only assess selectivity and efficacy of prosthetic stimulation through measurement of OOR responses. To interpret those OOR responses to prosthetic stimulation, we created a back-projecting, reverse prediction model relating eye movement responses of normal animals to the azimuth of the Earth-horizontal tilt axis that elicited similar OOR responses during natural tilt stimulation of normal chinchillas (Hageman et al. 2020). Those data revealed cosine dependence of each 3D OOR component on head tilt axis azimuth, so the reverse prediction uses an arccosine to estimate equivalent tilt axis from OOR data. To achieve a one-to-one mapping from OOR response data (whether the training set of normal OOR data used to create the model or OOR data elicited by prosthetic stimuli) to the azimuth of an Earth-horizontal equivalent head tilt stimulus axis that yields similar OOR responses in normal chinchillas, more than one ocular countertilt component is required as an input to the back-projection mapping, because arccosine functions are periodic and otherwise would not yield a unique azimuth estimate.

Further analysis of the results shown in Fig. 11 in the companion paper (Hageman et al. 2020) showed the general trends listed in Table 1. One can quickly narrow down the "group" of potential tilt axes using the *binocular* sign of the roll and pitch components (+ or −) in addition to the ratio of magnitudes of right eye/the left eye. Since all data were acquired with the *Z*-axis initially Earth-vertical, the yaw

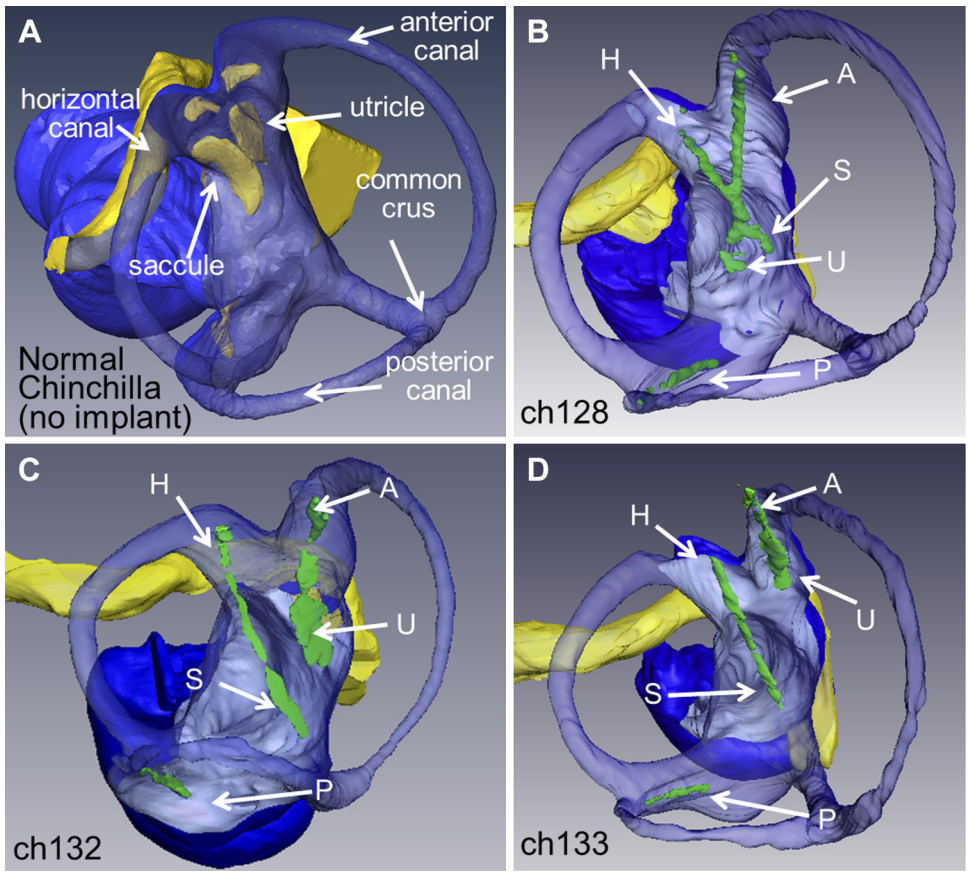

Fig. 5. *A*: postmortem microcomputed tomograhy scans for each of the 3 implanted chinchillas with the normal MRI image are labeled for comparison (Hayden et al. 2011). The scan at 32-μm resolution was segmented in Amira (FEI Visualization Sciences Group, Bordeaux, France). Blue: lumen; yellow: facial nerve; green: electrode array: each array is labeled based on the intended target as follows: H, horizontal semicircular canal; A, anterior (or superior) canal; P, posterior canal; U, utricle; and S, saccule. The posterior canal array was well placed in all 3 animals. *B*: for *Ch128*, the horizontal and superior canal electrodes were well positioned, but their trajectories were such that the utricle and saccule arrays overlapped in the vestibule. *C*: *Ch132* had excellent placement of the horizontal canal, superior canal and utricular arrays, but the saccule array overshot its target end organ. *D*: *Ch133* had the best saccule placement of the three animals, and the inferior half of utricle array was near the utricular macula and nerve.

component was not included in the table. There is large variation seen in the small yaw component and thus it was not useful for prediction of tilt axis from eye movement data. Table 1 does not present absolute requirements for each data group; instead, the table focuses on the polarity of the median ocular countertilt for each tilt axis to indicate the trend of the data.

A linear mixed-effect model was created to relate 3D binocular OOR data from Hageman et al. (2020) for normal chinchillas to the azimuths of Earth-horizontal head tilt axes for head tilts that elicited those OOR responses. The model's three input variables are as follows:

1) The interaction between the sign of the right eye's normalized pitch component [sign(norm_RY)] and the arccosine (in degrees) of right eye's normalized roll component (norm_RX)-180;

2) The interaction between the sign of the left eye's normalized pitch component [sign(norm_LY)] and the arccosine (in degrees) of left eye's normalized roll component (norm_LX)-180; and

3) The ratio of right/left eye ocular counter-roll magnitude (magRatio).

The resulting model equation was as follows: azimuth of Earth-horizontal tilt axis = $a + (b \times \text{magRatio}) + c \times \text{sign(norm\_RY)} \times [\arccos(\text{norm\_RX}) - 180] + d \times \text{sign(norm\_LY)} \times \arccos(\text{norm\_LX-180})$. The model incorporates each chinchilla as a conditional variable to account for any animal-specific variations in the eye responses. The prediction fit the normal data set (Hageman et al. 2020) with an adjusted $R^2 = 0.65$. Each of the included input variables and interactions of variables are statistically significant in predicting the azimuth of Earth-horizontal tilt axis ($P < 0.01$ for all). Model parameters a, b, c, and d are listed in Table 2.

RESULTS

The large number of electrodes implanted made testing every possible electrode combination with every possible stimulus parameter impractical within the test session duration that

Table 1. *The polarity of normalized left and right eye components of ocular countertilt response based on the grouped tilt axes*

Data Group	Tilt Axis	Right-Eye Roll	Left-Eye Roll	Right-Eye Pitch	Left-Eye Pitch	Magnitude Ratio
1	−30°, −45°, −60°	−	−	+	+	L > R
2	−120, −135, −150°	+	+	+	+	L < R
3	120, 135, 150°	+	+	−	−	L > R
4	30, 45, 60°	−	−	−	−	L < R
5	Nose up (−90°)	+	−	+	+	R = L
6	Nose down (90°)	−	+	−	−	R = L
7	Right ear down (0°)	−	−	−	+	R = L
8	Left ear down (180°)	+	+	+	−	R = L

Data based on Tilt Axis column. Trends found using the median responses of data shown in Fig. 11, *C* and *D*, of the companion paper (Hageman et al. 2020).

Table 2. *Fit parameters to predict tilt axis from binocular eye movements*

Fit Parameter	Fixed Effect (independent variable)	Parameter Estimate	Standard Error	*t* Statistic	*P* value
a	(Intercept)	16.74	5.59	3.0	0.003
b	magRatio	−8.91	3.46	−2.57	0.01
c	acosdNRX:sgnRY	0.13	0.034	3.91	1.1e-4
d	acosdNLX:sgnLY	0.74	0.034	21.71	1.6e-71

Model parameters for the linear mixed effect model of the form: $y = a + (b \times \text{magRatio}) + c \times \text{sign(norm\_RY)} \times [\arccos(\text{norm\_RX}) - 180] + d \times \text{sign(norm\_LY)} \times \arccos(\text{norm\_LX-180})$, to predict the tilt axis using fixed effects (or input variables) of magRatio = ratio of right/left eye absolute magnitude of ocular counterroll position, acosdNRX:sgnRY = sign(normalized pitch of right eye) × [arccos(normalized roll of right eye in degrees–180)], and acosdNLX:sgnLY = sign(normalized pitch of left eye) × arccos-[normalized roll of left eye in degrees – 180)].

an animal could tolerate. Therefore, instead of comprehensively characterizing responses to every possible combination in this initial implementation of prosthetic utricle and saccule stimulation, we focused on addressing six goals. First, we sought to replicate results of canal stimulation with the new system, to confirm that the new electrode arrays and recording system yielded results comparable to our published studies on canal stimulation using Pt/Ir wire electrodes. Second, we sought to determine whether it is possible to generate a sustained ocular countertilt response during constant-rate pulse train stimulation, and if so, whether responses increase predictably and reliably with pulse rate and/or pulse amplitude. Third, we sought to determine whether electrical stimulation targeting the utricle and saccule elicits responses with temporal dynamics that differ from responses to electrical stimulation targeting the canals. Fourth, we sought to characterize the range of ocular countertilt response directions one can achieve with unilateral electrical stimulation of the left ear. Fifth, we sought to determine whether one can selectively stimulate different macular regions, as manifested by eliciting different ocular countertilt directions during stimulation via different electrodes near the maculae. Finally, we sought to contrast responses for a given stimulating electrode using three different reference electrodes: *1*) a *distant reference* (Pt/Ir wire implanted outside the temporal bone, in suboccipital musculature); *2*) a *common crus reference* (Pt/Ir wire implanted in the common crus near its junction with the vestibule); and *3*) a *near bipolar reference*, which refers to a neighboring electrode located on the same end organ's stimulating electrode array. The presentation described below is organized around those six goals.

Replication of natural and electrically evoked angular VOR. To test the oculographic recording system, we first measured natural aVOR responses to whole body rotation, for comparison with normative data (Della Santina et al. 2007). Figure 6, *A–C*, illustrates the normalized axis of aVOR velocity during 1-Hz sinusoidal whole body rotations at peak 30°/s velocity, about the axis of each canal, recorded after each animal was implanted with a head cap, head post, and scleral eye coils but before electrode implantation. Each axis shows the response during a leftward rotation. Although right eye responses to LARP rotation for *Ch128* and *Ch133* depart from the LARP axis (indicating possible restriction from scleral coil placement), the majority of measured data align well with the expected 3D aVOR response. These data are therefore sufficiently similar to published normal aVOR responses in chinchillas (Della Santina et al. 2007; Migliaccio et al. 2010) to confirm integrity and performance of scleral coils and recording system.

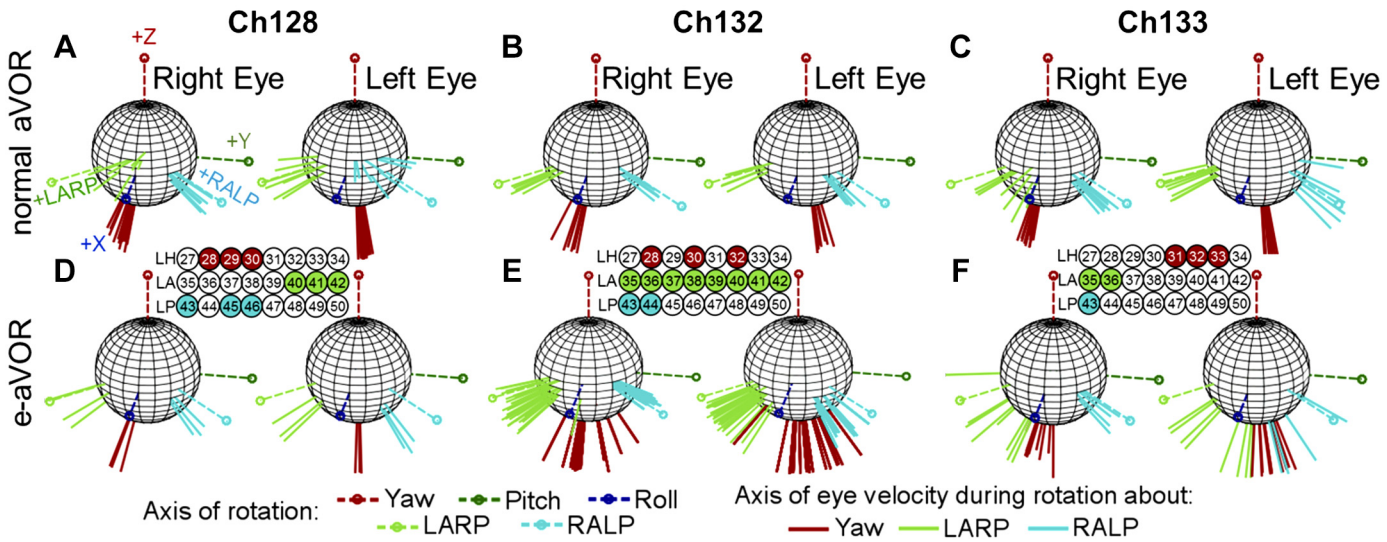

Fig. 6. Electrically evoked angular vestibulo-ocular reflex (aVOR) from 3 chinchillas. *A–F*: to test whether the new electrode array and circuitry could replicate previous results to restore the angular VOR (Dai et al. 2011a; Della Santina et al. 2007), we compared normal eye movements collected before electrode implant (*A–C*) to electrically evoked eye movements (*D–F*) using electrode arrays targeting semicircular canals. Each spherical plot shows the normalized axes of rotation, Yaw, left-anterior/right-posterior (LARP), right-anterior/left-posterior (RALP), Pitch, and Roll. The axes represent the axis of eye velocity during a left-ward head movement for the normal data. In general, the axis of eye rotation is aligned with the axis of rotation (the canal axis). However, for *Ch128* and *Ch133*, the right eye LARP response shows misalignment, which is possibly due to slight tethering from the scleral coil. For the electrically evoked aVOR (e-aVOR; *D–F*), each axis represents the normalized axis of eye velocity during peak positive stimulation. The rows of electrodes represent the 8 electrode contacts for the left horizontal (LH), left anterior (LA), and left posterior (LP) canals. Highlighted electrodes represent the contacts that elicited the best results within that canal.

Figure 6, *D–F*, shows the normalized electrically evoked aVOR elicited during electrical stimulation on the highlighted electrodes (LH: left horizontal; LA: left anterior; and LP: left posterior canals), all using a common crus reference, in the same animals after electrode implantation. For these experiments, the animal was stationary in darkness, so eye movements shown here represent responses solely driven by electrical stimulation. Every electrode in *Ch132*'s LA electrode array elicited well-aligned responses, but generally the most effective electrodes for each canal tended to be a smaller set of neighboring electrodes nearest the target ampulla. For *Ch132*, the lead to electrode 29 was broken and could not be used for LH stimulation. Stimuli delivered via *Ch133*'s LA electrodes elicited yaw eye movements for higher currents, likely due to spread of stimulus current toward the LH ampullary nerve. Overall, these results confirm that the flexible planar canal electrode arrays used in this study can elicit electrically evoked aVOR responses similar to those we have observed in prior experiments using Pt/Ir wire electrodes inserted into each ampulla (Dai et al. 2011a; Della Santina et al. 2007; Fridman et al. 2010).

Electrically evoked ocular countertilt. Figure 7 shows example electrically evoked eye movements during a 40-s pulse train at 300 pps presented to one utricular electrode pair (stimulating *electrode 20* and reference *electrode 15*, see Fig. 2 for electrode schematic) at different amplitudes shown by the different color lines. The shaded area in gray indicates the time when stimulation was on. As the pulse amplitude was increased, the magnitude of angular eye position also increased while maintaining the same direction of ocular countertilt throughout the five trials of amplitude variation. Similarly, Fig. 8 shows the electrically evoked eye movement during a 40-s pulse train using 100-μA pulses at varying pulse rates from 50 to 300 pps. These examples were collected using stimulating *electrode 20* and reference *electrode 19*, both on/near the utricle (see Fig. 2 for electrode numbers), with the stimulation period indicated by the gray shading on the plot. As the pulse rate increased, the change in angular position also increased for the eight trials of pulse rate variation. These pulse rate and current amplitude sweeps were completed on a subset of electrode combinations in each animal.

Temporal dynamics of canal versus otolith stimulation. Figure 9 illustrates a comparison between a 40-s step in pulse rate (200 pps) delivered via canal electrodes with a common crus reference and a 40-s step in pulse rate (300 pps) delivered via utricle- or saccule-targeting electrodes with either distant, common crus, or near bipolar references. Figure 9, *A–N*, displays both the right (Fig. 9, *A*, *C*, *E*, *G*, *I*, *K*, and *M*) and left (Fig. 9, *B*, *D*, *F*, *H*, *J*, *L*, and *N*) eye angular position over time. In the 74 trials across the three animals that delivered a pulse rate step change to SCC electrodes, a variety of responses were seen, as illustrated by three representative examples in Fig. 9, *A–F*. The first (Fig. 9, *A* and *B*, seen in 33/74 trials) shows prolonged nystagmus seen at the onset of the stimulation that begins to decay over time with an increase again at stimulation offset. The second (Fig. 9, *C* and *D*, seen in 31/74 trials) shows an eye movement response similar to an ocular countertilt (with the addition of quick phases), with a rapid initial change in angular eye position that is held throughout the 40-s stimulus (although generally decaying over time), possibly indicative of current spread to the utricle or saccule. The third example (Fig. 9, *E* and *F*, seen in 10/74 trials) shows a fast adapting nystagmus at the onset of stimulation, typical of a canal-mediated aVOR response to electrical stimulation targeting the canal.

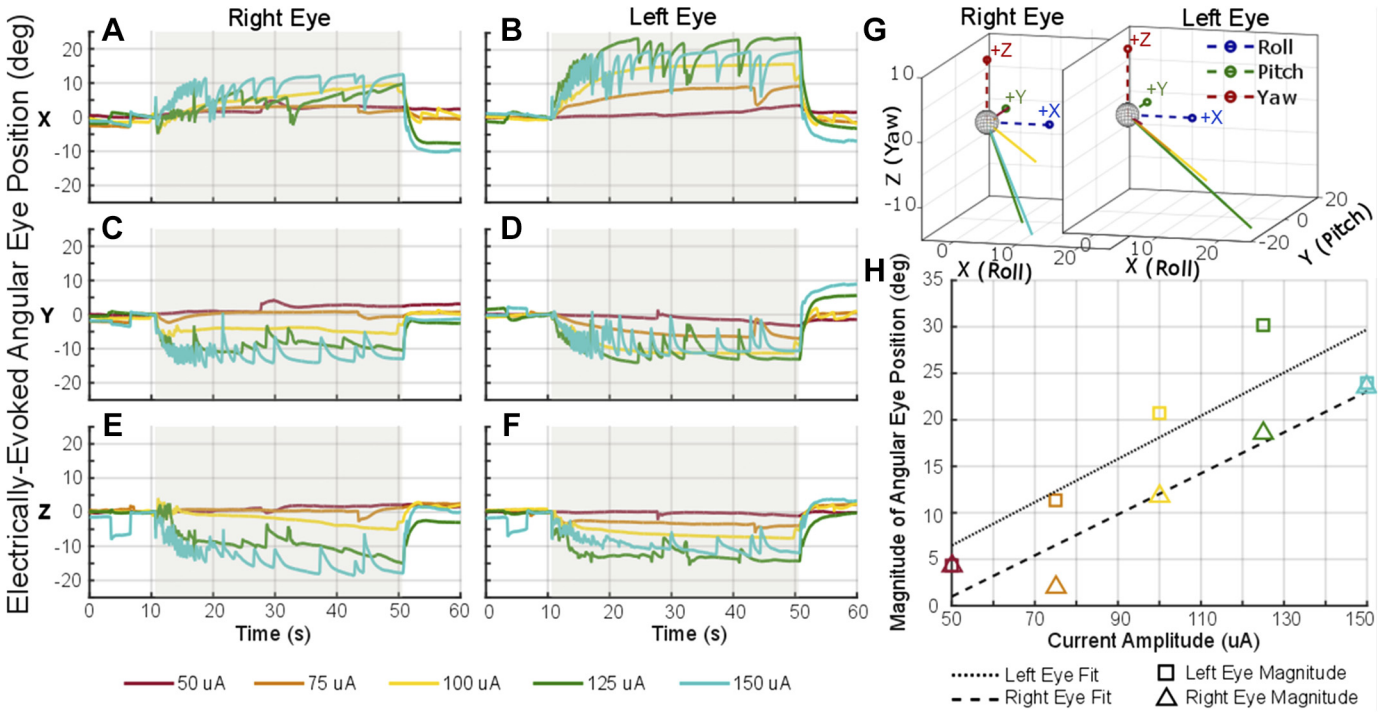

Fig. 7. Electrically evoked ocular countertilt with stimulation of increasing pulse amplitude. Example data from *Ch133* during a constant-rate pulse train using the same "near bipolar" pair of electrodes in the utricle, stimulating *electrode 20* and reference *electrode 15*. *A–F*: the stimulation was on for 40 s (gray shaded area) with a pulse rate of 300 pps. Biphasic pulse was 100 μs per phase with a 50-μs interphase gap. *G* and *H*: as the current amplitude was increased for each trial, a larger ocular countertilt response was elicited (*H*) with consistent direction of eye response (*G*).

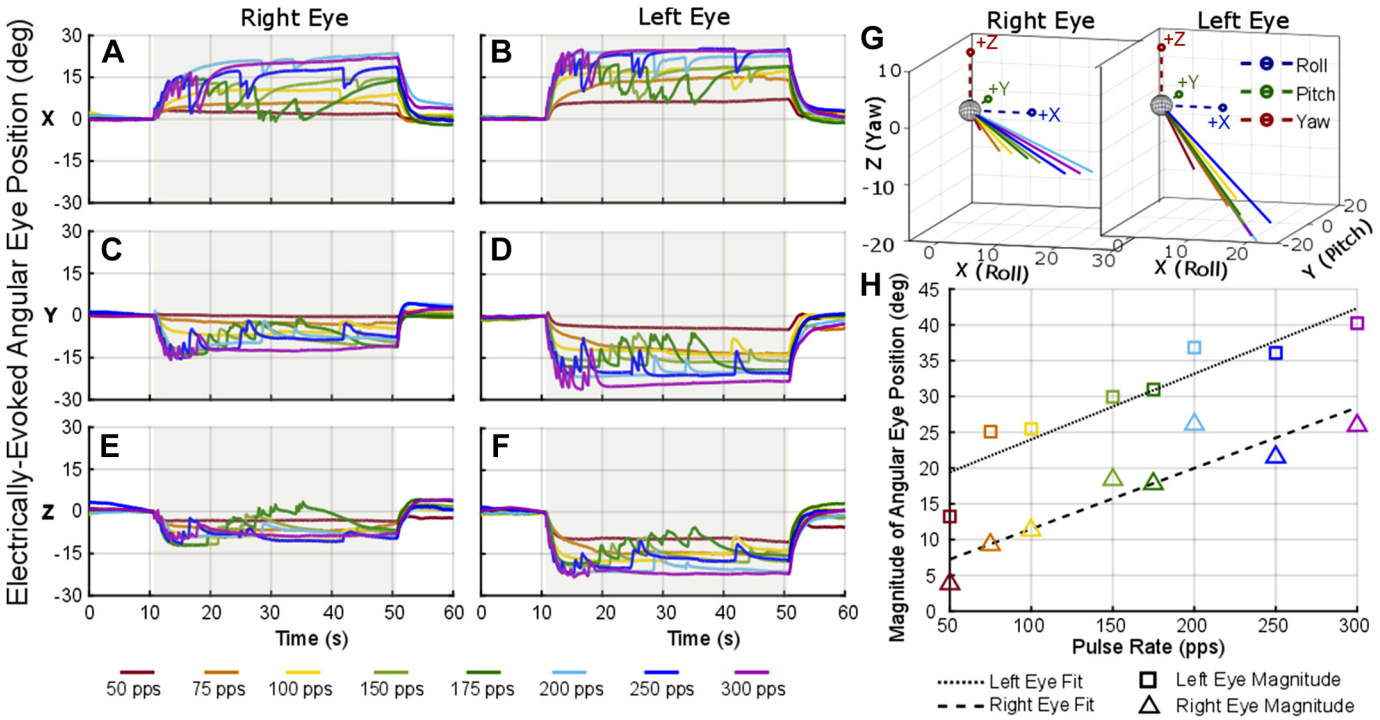

Fig. 8. Electrically evoked ocular countertilt with stimulation of increasing pulse rate. Example data from *Ch133* during a constant-rate pulse train using the same "near bipolar" pair of electrodes in the utricle, stimulating *electrode 20* and reference *electrode 19*. *A–F*: the stimulation was on for 40 s (gray shaded area). Each biphasic pulse was 100 μs per phase with a 50-μs interphase gap and 100-μA amplitude. *G* and *H*: as the pulse rate was increased for each trial, a larger ocular countertilt response was elicited (*H*) with consistent direction of eye response (*G*).

Eye movements elicited by a pulse train stimulus delivered via utricle and/or saccule electrodes varied in temporal dynamics depending on the location of the reference electrode. Figure 9, *G* and *H*, shows a representative example of an electrically evoked response during a constant-rate pulse train with a distant reference electrode (trend seen in 119/135 of distal reference combinations). A change in eye position happens immediately upon stimulation onset, and the position is held for the duration of the stimulation. When using a common crus reference (representative trace shown in Fig. 9, *I* and *J*), the eye position also generally changes right at onset but then continues to grow a small amount to settle at the final angular eye position (trend seen in 90/130 of common crus reference combinations). Finally, when using a near bipolar reference, two different time courses were seen (in addition to the time course shown in Fig. 7 and Fig. 8, which accounted for 140/421 cases of bipolar otolith-targeted stimulation): either a slow rise time to the final position (Fig. 9, *K* and *L*, seen in 172/421 cases of bipolar otolith-targeted stimulation) or a delayed onset of change in angular eye position (Fig. 9, *M* and *N*, seen in 109/421 cases of bipolar otolith-targeted stimulation).

To compare differences in the timing of responses as a function of reference electrode category for utricle and saccule stimulation, a comparison between rise times to final angular eye position was completed and is shown in Fig. 10. All utricle and saccule constant-rate pulse train trials were pooled into three groups: distant reference, common crus reference, and near bipolar reference. Additionally, a fourth group for SCC-targeted stimulation using common crus and distant reference was added for comparison of responses elicited from SCC-targeted versus otolith-targeted electrodes. The time to reach 63% of the final angular eye position was calculated for each component of the angular eye position (yaw, pitch, and roll) for each eye. If one component of the eye movement changed $<1°$ throughout the trial, it was excluded from this calculation. The spread of rise time for utricle/saccule stimulation using the near bipolar configuration is noticeably larger than utricle/saccule stimulation using distant and common crus reference and larger than semicircular canal stimulation. A Kruskal-Wallis test showed significance within each component of each eye. Post hoc Wilcoxon rank sum tests determined a significant difference ($P < 0.001$) between the rise time for near bipolar paradigms and that for the corresponding distant and common crus references for all components of eye movement in both eyes. The delayed reaction and slower rise time of eye movement using the *near bipolar* reference is comparable to that reported by Baarsma and Collewijn (1975) in normal rabbits during linear track accelerations.

Spatial selectivity of ocular response from otolith stimulation. Figure 11 illustrates the nonnormalized electrically evoked eye movements from all constant-rate pulse trains delivered via a utricular electrode (*first 2 columns*) or saccular electrode (*last 2 columns*) for each chinchilla that elicited a response above a 1° eye movement. In total, 421/1214 near bipolar electrode pairs, 130/250 common crus reference pairs, and 135/217 distal reference pairs were selected for analysis. The remaining trials tested were on an electrode pair that did not elicit a response due to either poor connectivity between the stimulator and the electrode or poor contact between the electrode and the nerve ending. Each vector indicates the yaw, pitch and roll components of the mean 3D angular position during the last 5 s of each 40-s pulse train and is color coded to signify the corresponding stimulating electrode, shown in the legend. The yaw, pitch, and roll coordinate system axes are plotted with a

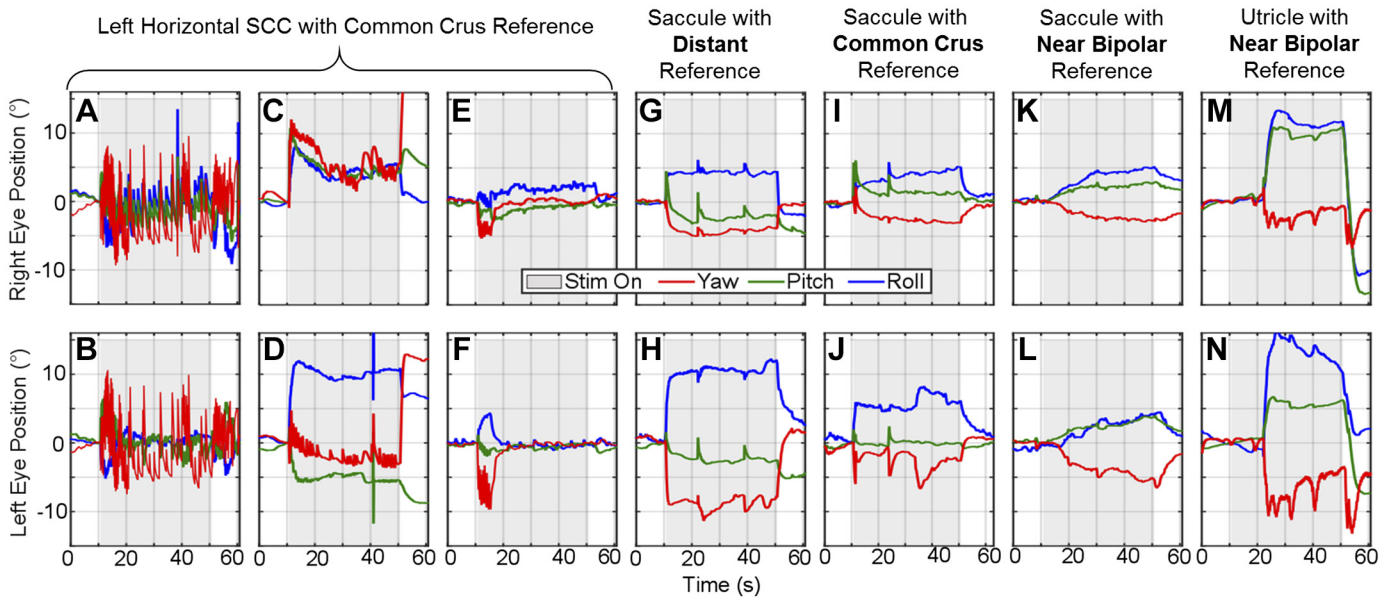

Fig. 9. Electrically evoked ocular countertilt using different reference electrodes. Example ocular countertilt responses during constant-rate pulse train stimulation applied to difference combinations of electrodes. *A–F*: 3 different types of responses seen when delivering a step change in pulse rate of 200 pps to a semicircular canal electrode with common crus reference. Although each example is recorded from a different chinchilla, all examples are representative of responses seen in each animals. The 1st example (*A* and *B*, *Ch133*) shows immediate onset of quick phases that begin to adapt out throughout the 40 seconds of stimulation, with an increase of frequency after stimulation stops. The 2nd example (*C* and *D*, *Ch132*) appears to follow the trend of an ocular countertilt, suggesting likely current spread to the otolith end organs (31/74 trials). The 3rd example (*E* and *F*, *Ch128*) shows a brief change in eye movement at the beginning of stimulation that quickly adapts out. The final examples compare the canal response to otolith and show representative examples of a pulse train (300 pps) delivered to the utricle and saccule stimulation with distant (*G* and *H*, *Ch128*), common crus (*I* and *J*, *Ch128*), and near bipolar (*K* and *L*, *Ch128*; and *M* and *N*, *Ch132*) references. Stimulation using distant reference elicited immediate change in angular eye position, similar to that seen during normal whole body static tilt. The saccule with common crus example follows a similar trend with immediate change in eye position but a slower incline to the final angular eye position. Using a near bipolar reference elicited 2 different types of responses: *1*) a slow gradual increase in angular eye position, following the low-pass filter behavior of the otolith end organs, and *2*) a delayed sudden change in angular eye position after stimulation onset.

magnitude of 10°. Figure 11, *bottom row*, shows the ocular countertilt responses recorded from six normal chinchillas (with 3 of the 6 being *Ch128*, *Ch132*, and *Ch133* before electrode implantation) during 20° whole body static tilts about the indicated axes as described in the companion paper (Hageman et al. 2020).

Comparison of electrically evoked OOR responses to these normal data provide a context within which one can begin to infer the head motion or tilt that is effectively represented by the vestibular nerve activity elicited during electrical stimulation. (Note however that this interpretation is subject to the caveat that only one labyrinth is being electrically stimulated, while the contralateral labyrinth presumably reports that the head is neither moving nor oriented differently than it was before the onset of electrical stimulation.) Ocular countertilt responses of normal chinchillas during the whole body static tilts are disconjugate (i.e., the right and left eye responses differ in magnitude) when a whole body tilt is about an Earth-horizontal axis close to the resting optic axis of either eye as described in the companion paper (Hageman et al. 2020). For example, whole body tilt of a normal chinchilla about an Earth-horizontal axis close to the optic axis of the right eye (−30, −45, −60, 120, 135, and 150°) elicits a larger left eye response magnitude than right eye and thus a ratio of right eye magnitude/left eye magnitude of <1. A tilt about an axis oriented through the left eye (30, 45, 60, −120°, −135, and −150°) elicits a larger right eye magnitude than left and thus a ratio >1. Tilts about the anteroposterior and interaural axes (0, 90, 180, and −90°) give a ratio ≈1.

For the electrically evoked OOR responses to left-ear prosthetic stimulation in Fig. 11, the magnitude of left eye response is generally larger than the right eye, corresponding to the responses of normal animals to a tilt about an axis through the right eye (−30 to −60° or 120 to 150°). Further comparison to the direction of normal eye movements shows that the electrically evoked responses for all chinchillas seem to be mostly aligned with normal eye responses to tilts about Earth-horizontal axes at azimuth 120 to 150°. The data for *Ch128* follow similar trends for utricle and saccule, corresponding to expected results based on the overlapping utricle and saccule electrode placement shown in Fig. 5. Responses to electrical stimulation targeting the saccule in *Ch132* and *Ch133* differ from responses to electrical stimuli targeting the utricle. Saccule-targeted electrodes elicited responses with a greater tendency toward the axes of ocular countertilt that normally encode whole body tilts about axes that are Earth-horizontal and −150 to −120° from the +*x*-axis, whereas the responses from utricle targeted electrodes tended to correspond to axes +120 to +150° from the +*x*-axis.

We investigated which electrodes elicited which OOR eye movements by grouping eye movements according to the magnitude ratio of right/left eye position. Figure 12 shows an image of the utricle and saccule array for each chinchilla, with electrodes colored according to the ratio of right/left eye rotation magnitude (*group A*: ratio <0.8 red; *group B*: 0.8 ≤ ratio ≤ 1.2 yellow, and *group C*: ratio >1.2 blue). Trials where the magnitudes of eye movement for both eyes were <2° were eliminated. Each colored circle represents the cathodic-first stimulating electrode (from a near-bipolar pair) used to elicit

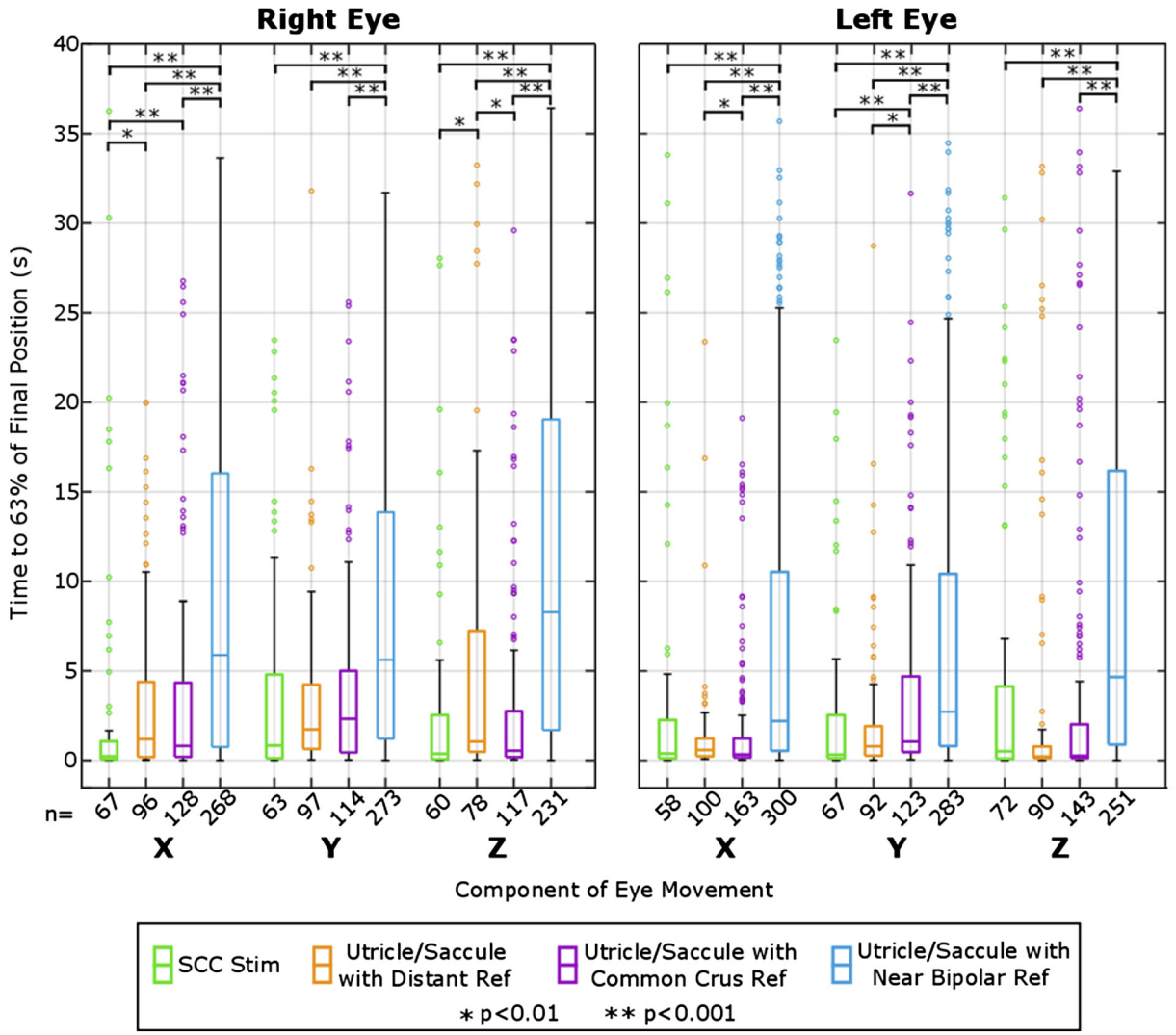

Fig. 10. Analysis of electrically evoked ocular counter tilt rise time grouped by reference type. Analysis of rise time to 63% of final ocular countertilt position for each component of each eye for 4 groups of data: *1*) semicircular canal (SCC) stimulation using common crus and distant reference, *2*) utricle/saccule stimulation using distant reference, *3*) common crus reference, and *4*) near bipolar reference. Components that showed <1° change in angular position were not used for this analysis, which is why there is a difference in number of samples (*n*), listed along the *x*-axis. An initial Kruskal-Wallis test showed significance between the reference groups for all groups (Right *X*, Right *Y*, Right *Z*, Left *X*, Left *Y*, Left *Z*) with all $P < 0.001$. Subsequent pairwise Wilcoxon rank sum tests showed significance between utricle/saccule Near Bipolar Reference compared to Distant, Common Crus, and SCC stimulation with all $P < 0.001$.

OOR eye movement. This analysis revealed no clear pattern for *Ch128* or *Ch132* (Fig. 12); however, for *Ch133*, electrodes in *group A* (i.e., elicited a right eye positional magnitude/left eye positional magnitude ratio <0.8, meaning the left eye movement exceeded right eye movement by at least 20%) cluster toward the bottom part of the utricular targeted array. Although few examples of Reye/Leye ratio > 1.2 (*group C*) were observed for stimulation targeting the utricle, the ones that do occur cluster toward top part of the array. The clusters of electrodes that elicit eye movements in the same group suggest semiselective stimulation in *Ch133*.

Tilt axis model output. As described in METHODS we created a back-projection model, based on data from normal chinchillas, to compute the azimuth of the Earth-horizontal whole body tilt axis for which tilting a normal animal would elicit a given set of OOR eye movement responses. Using the back-projection model to analyze OOR responses measured during prosthetic stimulation in the present study, we generated estimates of the Earth-horizontal head tilt axis azimuth that would elicit those eeOOR eye movement data if the eeOOR data were actually the natural OOR responses of a normal chinchilla to an actual head tilt about an Earth-horizontal axis. Figure 13 shows the model output (representing the whole body Earth-horizontal tilt axis about which a normal animal would be reoriented to elicit a given OOR eye movement pattern) grouped by otolith end organ (utricle: circles; saccule: triangles) and by the type of reference electrode. For comparison to normative data, gray diamonds illustrate the range of responses to natural whole body tilt stimuli measured for each animal before electrode implantation. For *Ch132* and *Ch133*, electrical stimulation targeting the utricle using distant or common crus reference electrodes yielded eeOOR responses that clustered around the responses a normal animal would exhibit during whole body tilts about axes at azimuth 90° to 150° from $+X$ (shown in Fig. 11, *bottom right*). In contrast, electrical stimulation targeting the saccule in those animals using distant and

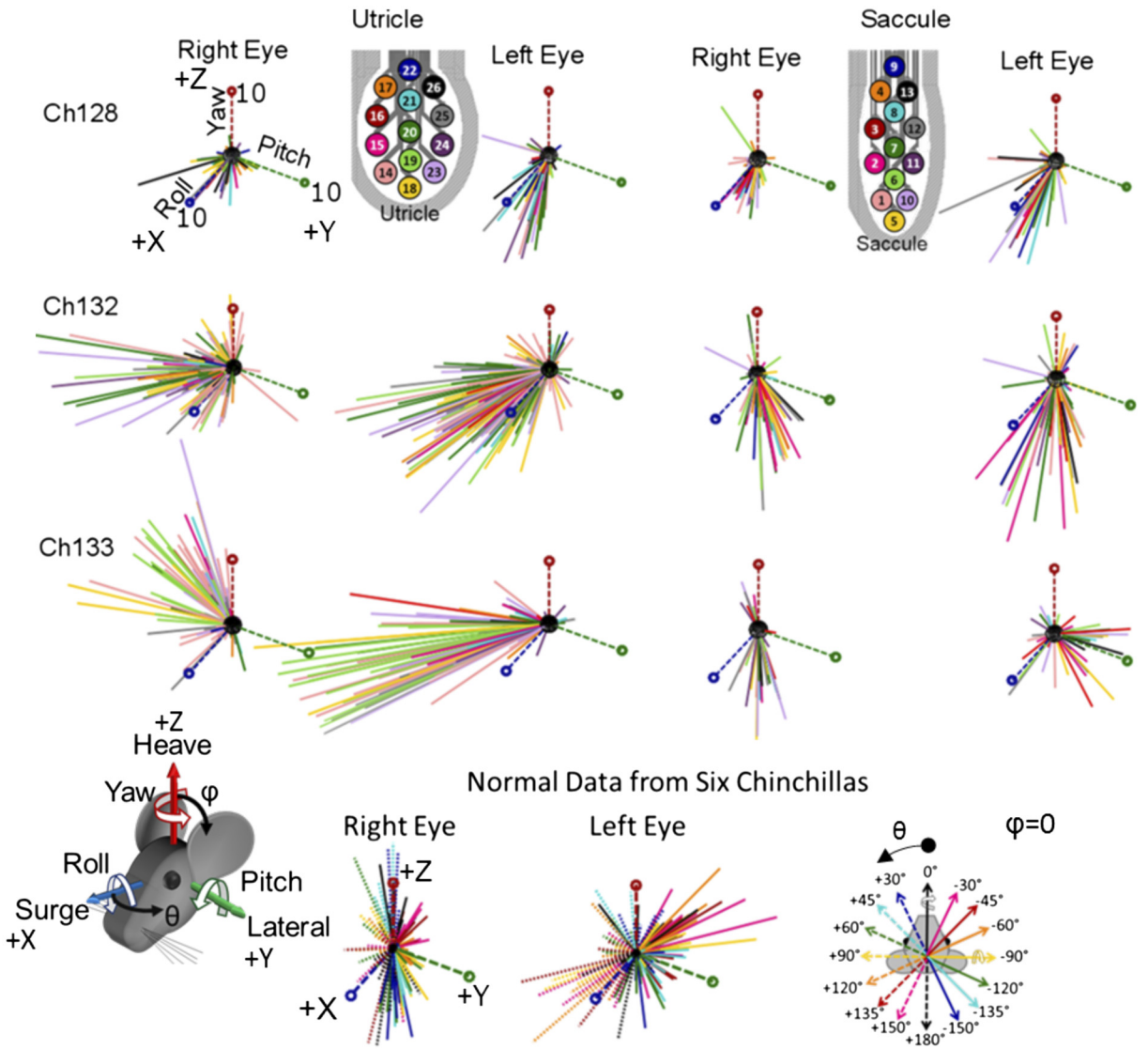

Fig. 11. All results from utricle and saccule pulse train stimulation for the 3 chinchillas. Each line represents the axis of the final angular eye position in degrees and is colored based on the stimulating electrode used, as indicated in the color-coded utricle and saccule electrodes in the bottom right. Each plot contains the primary axes, Roll (+X), Pitch (+*Y*), and Yaw (+*Z*), which are all magnitude of 10°, as shown in the top left image. *Bottom row*: final ocular countertilt position recorded from six normal chinchillas during 20° from horizontal whole body tilts about each of the axes in the legend, which follows the right-hand rule to indicate direction of tilt. By looking at all the nonnormalized responses, certain patterns of encoded head tilts with the stimulation data begin to emerge. With the use of the utricular array, the responses trend toward the (+*X*,−*Y*) quadrant with a larger left eye magnitude compared to the right. When comparing to the normal data (collected from the Earth-horizontal axes shown in the bottom right), the utricular responses primarily follow the +120, +135, and +150° axes. Shifting to the saccular data, for *Ch128*, responses due to saccular stimulation follow similar direction as the utricle. However, for *Ch132* and *Ch133*, a difference is seen between utricle and saccule responses. The left and right magnitudes are more symmetric and match the −120, −135, −150, and +180° normal tilt axes (solid green, light blue, dark blue, and dashed black).

common crus reference electrodes yielded eeOOR responses similar to those exhibited y normal animals during tilts about the −150 to −90° axes. For *Ch128*, a more uniform distribution of utricle versus saccule stimulation patterns was evident. Interestingly, use of a near-bipolar reference electrode (blue circles/teal triangles in Fig. 13) achieved, in *Ch128* and *Ch132*, a more diverse range of responses, signifying greater coverage of the range of normal tilt-OOR responses. This suggests that near bipolar stimulation, which should yield more spatially focal stimulation, can in fact achieve semiselective prosthetic stimulation of different regions on a macula.

CT imaging. Figure 5 shows 3D reconstructions of the electrode array locations in each of the three implanted animals, along with an analogous reconstruction of a microMRI for a normal chinchilla depicting neural elements (Hayden et al. 2011). Scan resolution was insufficient to show every thin film electrode individually; however, the arrays could be discerned in light of their known geometry and insertion trajectories through bone landmarks that were readily identified, such as the edges of the ampullotomies made surgically to gain access for insertion into the labyrinth. The posterior canal array was well positioned in all three animals. For *Ch128*, the horizontal and superior canal electrodes were well positioned, but their trajectories were such that the utricle and saccule arrays overlapped in the vestibule. *Ch132* had excellent placement of the horizontal canal, superior canal, and utricular

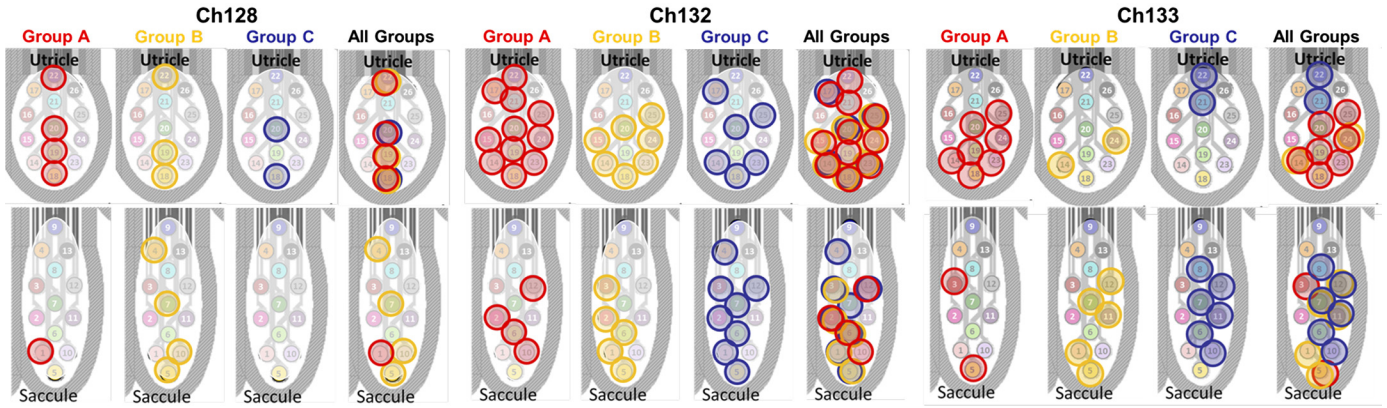

Fig. 12. Spatial selectivity of utricle and saccule stimulation. To examine spatial selectivity, the direction of eye movements elicited from stimulation can be grouped based on the magnitude ratio between the right and left eyes. From the ocular countertilt data collected from normal chinchillas detailed and shown in Fig 11, *bottom*, in the companion paper (Hageman et al. 2020) and using the trends in this manuscript's Table 1, the ratio of right/left eye magnitude gives an indication of the tilt axis in the following groups: *A*: ratio < 0.8 (right eye magnitude $<$ left eye magnitude); *B*: right and left eye magnitudes approximately equal ($0.8 \leq$ ratio ≤ 1.2); and *C*: ratio>1.2 (right eye magnitude $>$ left eye magnitude). Each stimulation electrode used to elicit eye movements are circled and grouped based on the magnitude ratio of eye position between the right and left eye. Data shown are from all chinchillas during 300 pps pulse train of 40-s duration, focusing on stimulation that elicited a change in angular eye position $>2°$ for both eyes. Focusing on *Ch133* only, for the utricular electrodes, the majority of eye movements showed a ratio <0.8 and were elicited more with the lower half of electrodes, circled in red. While only a few examples for *Ch133* where the ratio ≈ 1 or ratio >1.2, the examples for ratio>1.2, cluster toward the *top right*. Additionally, for the saccule of *Ch133*, clusters of red and blue sit on opposite sides of the array. This indicates that some level of selectivity may be achievable with proper placement. However, a similar pattern was not seen with *Ch128* and *Ch132*.

arrays, but the saccule array overshot its target end organ. *Ch133* had the best saccule placement of the three animals, and the inferior half of its utricle array was evidently near the utricular macula and/or nerve.

DISCUSSION

Compared with the relatively straightforward anatomy and physiology of the semicircular canals, the utricle and saccule pose numerous technical challenges to achieving spatially selective prosthetic stimulation that can effectively restore 3D sensation of gravitoinertial acceleration. Otolith stimulation attempts date back to 1891, when Breuer (1891) described failed attempts to selectively stimulate the saccule using a metal electrode, concluding that current inevitably spread to the nearby posterior canal ampulla, complicating attempts to discern what constituted an electrically evoked OOR. Decades

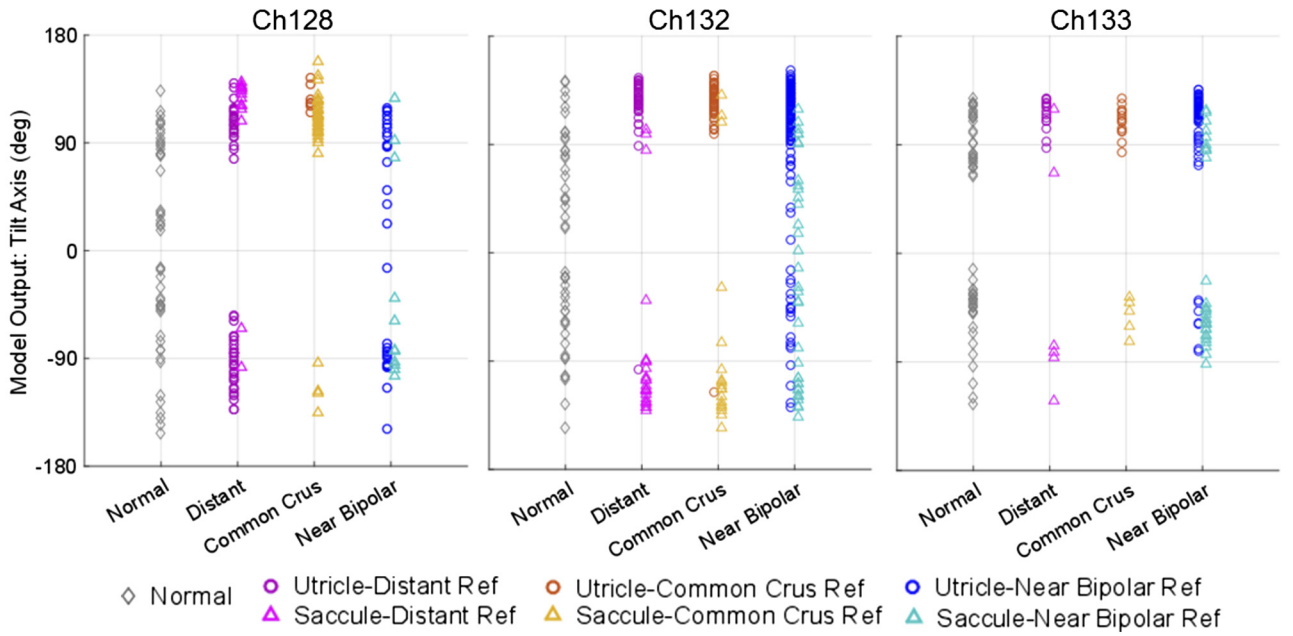

Fig. 13. Model output to infer electrically encoded tilt axis from electrically evoked eye movements. Estimated "encoded tilt axis" during stimulation on utricle (circles) and saccule (triangles) intended electrode contacts grouped by type of reference electrode. The normal eye movement output (gray diamonds) for each animal were collected before electrode implant. The model output was calculated based on the model discussed in METHODS. The results suggest that for *Ch132* and *Ch133* utricle stimulation with distant or common crus reference electrodes encodes primarily tilts about axes from $+90$ to $+150°$, where saccule stimulation with distant or common crus reference encodes primarily -90 to $-150°$ axes. For *Ch128*, there is less distinction between these sets of model output between utricle and saccule. With the use of a near bipolar reference electrode, the range of encoded tilt angles better represents the normal range.

later, Suzuki et al. (1969) electrically stimulated the utricular nerve in cats using short pulse trains (2–50 pulses) with 100–500 μs per pulse duration. During short bursts of stimulation, they observed rotation of both eyes, with upward shifts in the ipsilateral eye, downward in the contralateral eye, and small horizontal changes in eye position. Establishing standards for future attempts to stimulate the otolith end organs in strides to the like of Suzuki and Cohen for semicircular canal stimulation, Fluur and Mellström (1970a, 1970b, 1971) described attempts to stimulate the maculae in cats using 1-ms pulses of 200–800 mV at 300 pps and reported eye movements from visual inspection. They reported coordinated eye movements of compensatory direction based on the location of stimulation across the maculae. Attempting to replicate the results of Fluur and Mellström's, Curthoys (1987) used fine microelectrodes to electrically stimulate the utricular and saccular maculae in guinea pigs but found that the resulting eye movements always tended upward or up + torsional, independent of the stimulation location on the maculae. Subsequently, Goto et al. (2003, 2004) attempted to measure eye movements during electrical stimulation of the utricular and saccular nerve using metal wire electrodes implanted in cats. Attempts at selective utricular nerve stimulation generated mostly horizontal eye movements and attempts at selective saccular stimulation primarily yielded vertical eye movements, but effects due to current spreading to the ampullae could not be excluded.

Recently, Ramos de Miguel et al. (2017) reported initial attempts at utricular stimulation in humans. Three electrodes from a commercial cochlear implant were inserted temporarily in the vestibule near the utricle while attempts were made, with the patient under general anesthesia, to record far-field potentials the authors interpreted as electrically evoked compound action potentials from the electrode array and ocular vestibular evoked myogenic potentials (oVEMPs) for the contralateral eye. The significance of those findings regarding the goal of selectively stimulating the utricle and saccule to encode a 3D GIA is difficult to discern, because the oVEMP recording technique employed cannot measure eye movement direction. Moreover, the results should be considered in light of the fact that for oVEMP responses measured in normal alert animals are typically absent in the same subjects under general anesthesia (Yang et al. 2010).

We sought to explore the feasibility of overcoming utricle- and saccule-specific challenges and to address the ambiguous results of previous stimulation attempts with the aid of new, high-density planar electrode arrays and new data characterizing the 3D binocular otolith-ocular reflex responses of normal chinchillas. The flexible electrode arrays proved difficult to insert reliably, but when they were well positioned, we were able to generate electrically evoked OOR responses consistent with the OOR responses of normal animals to a wide range of head tilts. Responses grew predictably with increases in pulse rate and pulse amplitude. Responses using near bipolar electrode pairs, which we expected to provide the best chance at focal stimulation of macular regions, did yield responses consistent with focal activation of different parts of each macula. In contrast, stimulation via the same active electrode but returned via a more distant reference tended to elicit responses with temporal dynamics consistent with those expected for combined excitation of a combination of macular and canal afferents. Taken as a whole, these results support the feasibility of prosthetic stimulation of the utricle and/or saccule using this electrode fabrication process.

Several limitations of this study and the approach it employed merit discussion. First, the complexity and technical difficulty of these experiments limited the number of animals that could be tested with the available resources, which were limited by the supply of microfabricated electrode arrays. Nonetheless, although increasing the number of implanted animals could further enrich the data set provided here, the presented data are sufficient to address the goals that motivated this study, in that they demonstrate the feasibility of prosthetically stimulating the utricle and saccule and eliciting OOR responses signifying semiselective stimulation.

As evidenced by postmortem CT reconstructions used to assess electrode location, the planar geometry, flexibility, and compliance of the polyimide electrode arrays we employed made handling during surgery very challenging. This was exacerbated by the surgical approach we selected, which required that electrode arrays be inserted through the ampulla en route to the vestibule, despite the fact that surface tension on the meniscus of fluid that formed at the surface of each ampullotomy was great enough to deflect the arrays during insertion. Continued development of the electrode arrays should focus on adding a silicone stiffener at key points along the electrode array to allow for easier manipulation of the electrode during the implantation procedure.

Surgical technique could, and probably should, be revised to directly access the vestibule and lay the utricle and saccular arrays atop their targets under direct view; however, the likelihood of deafening the cochlea or damaging the paraflocculus of the cerebellum in chinchilla or rhesus with that approach is probably higher than the more conservative surgical approach we employed. Additionally, we wanted to minimize the number of independent leads based on previous vestibular implant experience, which indicated that implanting multiple individual leads could lead to the dislodging of already well-placed leads.

There are almost certainly effects due to current spread in the eye movements seen. This may explain the tendency of the eye movement responses to cluster around either the $+X,-Y$ quadrant or the $+X,+Y$ quadrant for the utricle and saccule, respectively, as current can easily travel to the associated anterior canal or posterior canal accordingly through the vestibule. However, by demonstrating that we can obtain both *1*) statistically significantly longer time constants, and *2*) eye movement responses that are not along the LA and LP axis, particularly when using bipolar stimulating/reference configurations compared with further reference electrodes, we believe we are at least mainly targeting current to the otolith end organs as intended. With any electrical stimulation within a fluid-filled space and using existing technology, some current spread and misalignment is to be expected.

Given animal use protocol constraints limiting the duration and number of test sessions per animal, the relatively long duration of each stimulus trial precluded testing of every possible stimulus current and pulse rate combination over every 1 of 364 stimulating/reference combinations available on the electrode arrays. We prioritized testing as many electrode combinations as possible within each animal to describe a spatial and temporal map of stimulated areas, and we therefore necessarily limited the number of repeated trials performed on

each electrode pair. Reliability and consistency of ocular responses to a given prosthetic stimulus over repeated presentations that span days or weeks merit further exploration, particularly given the possible influences of central nervous system compensation to prosthetic stimuli, which could include adaptation, habituation, and long-term depression.

The data presented were all collected in otherwise normal animals that had not been treated with ototoxic doses of gentamicin treatment to ablate hair cell function and induce vestibular sensory loss. Therefore, some spontaneous baseline neuronal firing was likely present in the implanted ear, and prosthetic electrical stimuli may have modulated primary afferent activity both via direct stimulation and indirectly through action on surviving hair cells. However, surgical implantation likely caused vestibular hypofunction on the implanted side due to significant labyrinthine trauma and disruption of the membranous labyrinth. The three animals all had a head tilt in their cage and a very slow spontaneous nystagmus while head-fixed in dark in the weeks following the surgery toward the side of the implant, indicating some damage may have occurred during implantation. Future studies can investigate histology to assess any tissue damage due to the implantation procedure. Moreover, electrical stimulation experiments were performed with the head stationary to prevent mechanical stimuli that could be transduced by residual hair cells and to thereby isolate effects due to the electrical stimulation alone. Finally, it is worth noting that in the human condition we hope ultimately to treat (e.g., hair cell injury due to gentamicin ototoxicity), type two hair cell bodies are likely to be present and sensitive to electrical stimulation (Sun et al. 2015).

Coupled with the fact that this study employed transient pulse train stimuli rather than both upward and downward modulation of pulse rate and/or amplitude about a nonzero tonic stimulus to which an animal is preconditioned, the presence of functional hair cells in the implanted ear also limited us to solely excitatory stimulation. Future explorations of prosthetic utricular and saccular stimulation should explore whether up- and downmodulation about a tonic baseline for stimuli delivered by near-bipolar utricular or saccular electrodes can elicit OOR responses signifying both excitation and inhibition, respectively, of a portion of the target macula.

Because the contralateral ear was normal, that labyrinth provided a signal incongruent with the prosthetic input. This may have limited the range of responses we could elicit, because the prosthetic signal delivered to the implanted labyrinth was always interpreted in conjunction with incompatible input from the contralateral labyrinth. Future exploration of prosthetic stimulation targeting the utricle and saccule should examine responses to complementary excitation and inhibition of both labyrinths.

To pare down the number of stimulation channels and the consequent complexity and size of the implanted stimulator required, future iterations of this work should try to define how many electrode contacts are needed based on the level of spatial selectivity one can reliably achieve. Judging from the data summarized in Fig. 12, the spread of stimulus current in the present study was such that no more than approximately four regions of a macula might be semiselectively addressable with electrodes like those we employed.

This work has focused on eye movements elicited by electrical stimulation targeting the utricle and saccule. However, the utricle and saccule also each play important roles in stabilizing head orientation, body posture, gait, autonomic functions, and spatial perception. Quantitative gait and postural testing in rodents is difficult to perform with precision comparable to 3D oculography, but assessment of otolith end organ stimulation on head tilt, which is often pronounced in chinchillas after acute unilateral labyrinthine injury, should be a feasible and informative functional assay.

ACKNOWLEDGMENTS

We acknowledge Kelly Lane for help with animal care and Taek-Soo Lee and Benjamin Tsui for indispensable help in obtaining the microcomputed tomography scans of each animal.

GRANTS

This work was supported by National Institute of Deafness and Other Communications Disorders (NIDCD) Grants R01-DC-009255 and T32-DC-000023. K. N. Hageman and M. R. Chow effort to develop equipment for use in this work was supported in part by NIDCD Grant R01-DC-014503. Electrode fabrication was performed under the auspices of the U.S. Department of Energy by Lawrence Livermore National Laboratory under Contract DE-AC52-07NA27344-LLNL-JRNL-764599.

DISCLOSURES

C. C. Della Santina holds an equity interest in Labyrinth Devices, LLC, which is working to develop a vestibular implant for clinical use through a collaboration with Johns Hopkins School of Medicine and Med-El, GmbH. The terms of that arrangement are managed in accordance with John Hopkins University policies on conflicts of interest and interaction with industry.

AUTHOR CONTRIBUTIONS

K.N.H., A.T., K.L., S.F., S.S.P., R.H., and C.C.D.S. conceived and designed research; K.N.H. and M.R.C. performed experiments; K.N.H. and M.R.C. analyzed data; K.N.H., M.R.C., P.J.B., D.R., and C.C.D.S. interpreted results of experiments; K.N.H. and M.R.C. prepared figures; K.N.H. drafted manuscript; K.N.H., M.R.C., A.T., and C.C.D.S. edited and revised manuscript; K.N.H., A.T., and C.C.D.S. approved final version of manuscript.

REFERENCES

Angelaki DE. Dynamic polarization vector of spatially tuned neurons. *IEEE Trans Biomed Eng* 38: 1053–1060, 1991. doi:10.1109/10.99068.

Angelaki DE. Two-dimensional coding of linear acceleration and the angular velocity sensitivity of the otolith system. *Biol Cybern* 67: 511–521, 1992. doi:10.1007/BF00198758.

Angelaki DE. Three-dimensional organization of otolith-ocular reflexes in rhesus monkeys. III. Responses to translation. *J Neurophysiol* 80: 680–695, 1998. doi:10.1152/jn.1998.80.2.680.

Angelaki DE, Hess BJ. Three-dimensional organization of otolith-ocular reflexes in rhesus monkeys. II. Inertial detection of angular velocity. *J Neurophysiol* 75: 2425–2440, 1996b. doi:10.1152/jn.1996.75.6.2425.

Angelaki DE, Hess BJ. Three-dimensional organization of otolith-ocular reflexes in rhesus monkeys. I. Linear acceleration responses during off-vertical axis rotation. *J Neurophysiol* 75: 2405–2424, 1996a. doi:10.1152/jn.1996.75.6.2405.

Angelaki DE, Newlands SD, Dickman JD. Inactivation of semicircular canals causes adaptive increases in otolith-driven tilt responses. *J Neurophysiol* 87: 1635–1640, 2002. doi:10.1152/jn.00775.2001.

Angelaki DE, Shaikh AG, Green AM, Dickman JD. Neurons compute internal models of the physical laws of motion. *Nature* 430: 560–564, 2004. doi:10.1038/nature02754.

Baarsma EA, Collewijn H. Eye movements due to linear accelerations in the rabbit. *J Physiol* 245: 227–247, 1975. doi:10.1113/jphysiol.1975.sp010842.

Boutros PJ, Schoo DP, Rahman M, Valentin NS, Chow MR, Ayiotis AI, Morris BJ, Hofner A, Rascon AM, Marx A, Deas R, Fridman GY, Davidovics NS, Ward BK, Treviño C, Bowditch SP, Roberts DC, Lane KE, Gimmon Y, Schubert MC, Carey JP, Jaeger A, Della Santina CC.

Continuous vestibular implant stimulation partially restores eye-stabilizing reflexes. *JCI Insight* 4: 128397, 2019. doi:10.1172/jci.insight.128397.

Breuer J. Über die function der otolithen-apparate. *Arch Physiol* 48: 195–306, 1891. doi:10.1007/BF01802737.

Carey JP, Della Santina C. Principles of applied vestibular physiology. In: *Cummings Otolaryngology: Head & Neck Surgery*. Philadelphia, PA: Mosby, 2005, p. 3115–3159.

Chiang B, Fridman GY, Dai C, Rahman MA, Della Santina CC. Design and performance of a multichannel vestibular prosthesis that restores semicircular canal sensation in rhesus monkey. *IEEE Trans Neural Syst Rehabil Eng* 19: 588–598, 2011. doi:10.1109/TNSRE.2011.2164937.

ClinicalTrials.gov. *ClinicalTrials.gov: Safety, Tolerability and Efficacy for CGF166 in Patients With Unilateral or Bilateral Severe-to-profound Hearing Loss* (Online). https://clinicaltrials.gov/ct2/show/NCT02132130?cond=cgf166&rank=1. [2018a].

ClinicalTrials.gov. *ClinicalTrials.gov: Multichannel Vestibular Implant Early Feasibility Study* (Online). https://clinicaltrials.gov/ct2/show/NCT02725463?cond=vestibular+implant&rank=1. [2018b].

Cohen B, Maruta J, Raphan T. Orientation of the eyes to gravitoinertial acceleration. *Ann N Y Acad Sci* 942: 241–258, 2001. doi:10.1111/j.1749-6632.2001.tb03750.x.

Curthoys IS. Eye movements produced by utricular and saccular stimulation. *Aviat Space Environ Med* 58: A192–A197, 1987.

da Cruz L, Dorn JD, Humayun MS, Dagnelie G, Handa J, Barale PO, Sahel JA, Stanga PE, Hafezi F, Safran AB, Salzmann J, Santos A, Birch D, Spencer R, Cideciyan AV, de Juan E, Duncan JL, Eliott D, Fawzi A, Olmos de Koo LC, Ho AC, Brown G, Haller J, Regillo C, Del Priore LV, Arditi A, Greenberg RJ. Five-year safety and performance results from the argus ii retinal prosthesis system clinical trial. *Ophthalmology* 123: 2248–2254, 2016. doi:10.1016/j.ophtha.2016.06.049.

Dai C, Fridman GY, Chiang B, Davidovics NS, Melvin TA, Cullen KE, Della Santina CC. Cross-axis adaptation improves 3D vestibulo-ocular reflex alignment during chronic stimulation via a head-mounted multichannel vestibular prosthesis. *Exp Brain Res* 210: 595–606, 2011a. doi:10.1007/s00221-011-2591-5.

Dai C, Fridman GY, Chiang B, Rahman MA, Ahn JH, Davidovics NS, Della Santina CC. Directional plasticity rapidly improves 3D vestibulo-ocular reflex alignment in monkeys using a multichannel vestibular prosthesis. *J Assoc Res Otolaryngol* 14: 863–877, 2013. doi:10.1007/s10162-013-0413-0.

Dai C, Fridman GY, Davidovics NS, Chiang B, Ahn JH, Della Santina CC. Restoration of 3D vestibular sensation in rhesus monkeys using a multichannel vestibular prosthesis. *Hear Res* 281: 74–83, 2011b. doi:10.1016/j.heares.2011.08.008.

Dai C, Fridman GY, Della Santina CC. Effects of vestibular prosthesis electrode implantation and stimulation on hearing in rhesus monkeys. *Hear Res* 277: 204–210, 2011c. doi:10.1016/j.heares.2010.12.021.

Davidovics NS, Fridman GY, Chiang B, Della Santina CC. Effects of biphasic current pulse frequency, amplitude, duration, and interphase gap on eye movement responses to prosthetic electrical stimulation of the vestibular nerve. *IEEE Trans Neural Syst Rehabil Eng* 19: 84–94, 2011. doi:10.1109/TNSRE.2010.2065241.

Davidovics NS, Fridman GY, Della Santina CC. Co-modulation of stimulus rate and current from elevated baselines expands head motion encoding range of the vestibular prosthesis. *Exp Brain Res* 218: 389–400, 2012. doi:10.1007/s00221-012-3025-8.

Davidovics NS, Rahman MA, Dai C, Ahn J, Fridman GY, Della Santina CC. Multichannel vestibular prosthesis employing modulation of pulse rate and current with alignment precompensation elicits improved VOR performance in monkeys. *J Assoc Res Otolaryngol* 14: 233–248, 2013. doi:10.1007/s10162-013-0370-7.

Della Santina CC, Migliaccio AA, Patel AH. A multichannel semicircular canal neural prosthesis using electrical stimulation to restore 3-d vestibular sensation. *IEEE Trans Biomed Eng* 54: 1016–1030, 2007. doi:10.1109/TBME.2007.894629.

Desai SS, Zeh C, Lysakowski A. Comparative morphology of rodent vestibular periphery. I. Saccular and utricular maculae. *J Neurophysiol* 93: 251–266, 2005. doi:10.1152/jn.00746.2003.

Fluur E, Mellström A. Utricular stimulation and oculomotor reactions. *Laryngoscope* 80: 1701–1712, 1970a. doi:10.1288/00005537-197011000-00005.

Fluur E, Mellström A. Saccular stimulation and oculomotor reactions. *Laryngoscope* 80: 1713–1721, 1970b. doi:10.1288/00005537-197011000-00006.

Fluur E, Mellström A. The otolith organs and their influence on oculomotor movements. *Exp Neurol* 30: 139–147, 1971. doi:10.1016/0014-4886(71)90228-7.

Fridman GY, Davidovics NS, Dai C, Migliaccio AA, Della Santina CC. Vestibulo-ocular reflex responses to a multichannel vestibular prosthesis incorporating a 3D coordinate transformation for correction of misalignment. *J Assoc Res Otolaryngol* 11: 367–381, 2010. doi:10.1007/s10162-010-0208-5.

Fridman GY, Della Santina CC. Progress toward development of a multichannel vestibular prosthesis for treatment of bilateral vestibular deficiency. *Anat Rec (Hoboken)* 295: 2010–2029, 2012. doi:10.1002/ar.22581.

Gianna CC, Gresty MA, Bronstein AM. Eye movements induced by lateral acceleration steps. Effect of visual context and acceleration levels. *Exp Brain Res* 114: 124–129, 1997. doi:10.1007/PL00005611.

Goldberg JM, Desmadryl G, Baird RA, Fernández C. The vestibular nerve of the chinchilla. V. Relation between afferent discharge properties and peripheral innervation patterns in the utricular macula. *J Neurophysiol* 63: 791–804, 1990a. doi:10.1152/jn.1990.63.4.791.

Goldberg JM, Desmadryl G, Baird RA, Fernández C. The vestibular nerve of the chinchilla. IV. Discharge properties of utricular afferents. *J Neurophysiol* 63: 781–790, 1990b. doi:10.1152/jn.1990.63.4.781.

Goldberg JM, Smith CE, Fernández C. Relation between discharge regularity and responses to externally applied galvanic currents in vestibular nerve afferents of the squirrel monkey. *J Neurophysiol* 51: 1236–1256, 1984. doi:10.1152/jn.1984.51.6.1236.

Goldberg JM, Wilson VJ, Cullen KE, Angelaki DE, Broussard DM, Buttner-Ennever J, Fukushima K, Minor LB. Physiology of the vestibular organs. In: *The Vestibular System: A Sixth Sense*. New York: Oxford University Press, 2012, p. 70–115.

Golub JS, Ling L, Nie K, Nowack A, Shepherd SJ, Bierer SM, Jameyson E, Kaneko CRS, Phillips JO, Rubinstein JT. Prosthetic implantation of the human vestibular system. *Otol Neurotol* 35: 136–147, 2014. doi:10.1097/MAO.0000000000000003.

Gong W, Haburcakova C, Merfeld DM. Vestibulo-ocular responses evoked via bilateral electrical stimulation of the lateral semicircular canals. *IEEE Trans Biomed Eng* 55: 2608–2619, 2008. doi:10.1109/TBME.2008.2001294.

Gong W, Merfeld DM. Prototype neural semicircular canal prosthesis using patterned electrical stimulation. *Ann Biomed Eng* 28: 572–581, 2000. doi:10.1114/1.293.

Goto F, Meng H, Bai R, Sato H, Imagawa M, Sasaki M, Uchino Y. Eye movements evoked by the selective stimulation of the utricular nerve in cats. *Auris Nasus Larynx* 30: 341–348, 2003. doi:10.1016/j.anl.2003.07.003.

Goto F, Meng H, Bai R, Sato H, Imagawa M, Sasaki M, Uchino Y. Eye movements evoked by selective saccular nerve stimulation in cats. *Auris Nasus Larynx* 31: 220–225, 2004. doi:10.1016/j.anl.2004.03.002.

Guyot JP, Perez Fornos A. Milestones in the development of a vestibular implant. *Curr Opin Neurol* 32: 145–153, 2019. doi:10.1097/WCO.0000000000000639.

Hageman KN, Chow MR, Boutros PJ, Roberts D, Tooker A, Lee K, Felix S, Pannu SS, Della Santina CC. Design of a vestibular prosthesis for sensation of gravitoinertial acceleration. *ASME J Med Devices-Transactions* 10: 10–11, 2016a.

Hageman KN, Chow MR, Roberts D, Della Santina CC. Binocular 3D otolith-ocular reflexes: responses of normal chinchillas to tilt and translations. *J Neurophysiol* 123: 243–258, 2020. doi:10.1152/jn.00882.2018.

Hageman KN, Kalayjian ZK, Tejada F, Chiang B, Rahman MA, Fridman GY, Dai C, Pouliquen PO, Georgiou J, Della Santina CC, Andreou AG. A CMOS neural interface for a multichannel vestibular prosthesis. *IEEE Trans Biomed Circuits Syst* 10: 269–279, 2016b. doi:10.1109/TBCAS.2015.2409797.

Haslwanter T. Mathematics of three-dimensional eye rotations. *Vision Res* 35: 1727–1739, 1995. doi:10.1016/0042-6989(94)00257-M.

Hayden R, Sawyer S, Frey E, Mori S, Migliaccio AA, Della Santina CC. Virtual labyrinth model of vestibular afferent excitation via implanted electrodes: validation and application to design of a multichannel vestibular prosthesis. *Exp Brain Res* 210: 623–640, 2011. doi:10.1007/s00221-011-2599-x.

Hullar TE, Della Santina CC, Hirvonen T, Lasker DM, Carey JP, Minor LB. Responses of irregularly discharging chinchilla semicircular canal vestibular-nerve afferents during high-frequency head rotations. *J Neurophysiol* 93: 2777–2786, 2005. doi:10.1152/jn.01002.2004.

Hullar TE, Williams CD. Geometry of the semicircular canals of the chinchilla (*Chinchilla laniger*). *Hear Res* 213: 17–24, 2006. doi:10.1016/j.heares.2005.11.009.

Krebs DE, Gill-Body KM, Riley PO, Parker SW. Double-blind, placebo-controlled trial of rehabilitation for bilateral vestibular hypofunction: preliminary report. *Otolaryngol Head Neck Surg* 109: 735–741, 1993. doi:10.1177/019459989310900417.

Leigh RJ, Zee DS. *The Neurology of Eye Movements* (4th ed.). New York: Oxford University Press, 2006.

Lewis R, Haburcakova C, Gong W, Lee D, Wall C 3rd, Thompson L, Merfeld D. Vestibular prosthesis tested in rhesus monkeys. *Annu Int Conf IEEE Eng Med Biol Soc* 2011: 2277–2279, 2011.

Lewis RF, Gong W, Ramsey M, Minor L, Boyle R, Merfeld DM. Vestibular adaptation studied with a prosthetic semicircular canal. *J Vestib Res* 12: 87–94, 2002–2003.

Lewis RF, Haburcakova C, Gong W, Lee D, Merfeld D. Electrical stimulation of semicircular canal afferents affects the perception of head orientation. *J Neurosci* 33: 9530–9535, 2013a. doi:10.1523/JNEUROSCI.0112-13.2013.

Lewis RF, Haburcakova C, Gong W, Makary C, Merfeld DM. Vestibulo-ocular reflex adaptation investigated with chronic motion-modulated electrical stimulation of semicircular canal afferents. *J Neurophysiol* 103: 1066–1079, 2010. doi:10.1152/jn.00241.2009.

Lewis RF, Nicoucar K, Gong W, Haburcakova C, Merfeld DM. Adaptation of vestibular tone studied with electrical stimulation of semicircular canal afferents. *J Assoc Res Otolaryngol* 14: 331–340, 2013b. doi:10.1007/s10162-013-0376-1.

Maruta J, Simpson JI, Raphan T, Cohen B. Orienting otolith-ocular reflexes in the rabbit during static and dynamic tilts and off-vertical axis rotation. *Vision Res* 41: 3255–3270, 2001. doi:10.1016/S0042-6989(01)00091-8.

Merfeld DM, Gong W, Morrissey J, Saginaw M, Haburcakova C, Lewis RF. Acclimation to chronic constant-rate peripheral stimulation provided by a vestibular prosthesis. *IEEE Trans Biomed Eng* 53: 2362–2372, 2006. doi:10.1109/TBME.2006.883645.

Merfeld DM, Haburcakova C, Gong W, Lewis RF. Chronic vestibulo-ocular reflexes evoked by a vestibular prosthesis. *IEEE Trans Biomed Eng* 54: 1005–1015, 2007. doi:10.1109/TBME.2007.891943.

Migliaccio AA, Minor LB, Della Santina CC. Adaptation of the vestibulo-ocular reflex for forward-eyed foveate vision. *J Physiol* 588: 3855–3867, 2010. doi:10.1113/jphysiol.2010.196287.

Migliaccio AA, Todd MJ. Real-time rotation vectors. *Australas Phys Eng Sci Med* 22: 73–80, 1999.

Mitchell DE, Dai C, Rahman MA, Ahn JH, Della Santina CC, Cullen KE. Head movements evoked in alert rhesus monkey by vestibular prosthesis stimulation: implications for postural and gaze stabilization. *PLoS One* 8: e78767, 2013. doi:10.1371/journal.pone.0078767.

Nie K, Ling L, Bierer SM, Kaneko CRS, Fuchs AF, Oxford T, Rubinstein JT, Phillips JO. An experimental vestibular neural prosthesis: design and preliminary results with rhesus monkeys stimulated with modulated pulses. *IEEE Trans Biomed Eng* 60: 1685–1692, 2013. doi:10.1109/TBME.2013.2241433.

Paige GD, Seidman SH. Characteristics of the VOR in response to linear acceleration. *Ann N Y Acad Sci* 871: 123–135, 1999. doi:10.1111/j.1749-6632.1999.tb09179.x.

Phillips C, Shepherd SJ, Nowack A, Nie K, Kaneko CRS, Rubinstein JT, Ling L, Phillips JO. Loss of afferent vestibular input produces central adaptation and increased gain of vestibular prosthetic stimulation. *J Assoc Res Otolaryngol* 17: 19–35, 2016. doi:10.1007/s10162-015-0544-6.

Phillips JO, Ling L, Nie K, Jameyson E, Phillips CM, Nowack AL, Golub JS, Rubinstein JT. Vestibular implantation and longitudinal electrical stimulation of the semicircular canal afferents in human subjects. *J Neurophysiol* 113: 3866–3892, 2015. doi:10.1152/jn.00171.2013.

Phillips JO, Ling L, Nowack AL, Phillips CM, Nie K, Rubinstein JT. The dynamics of prosthetically elicited vestibulo-ocular reflex function across frequency and context in the rhesus monkey. *Front Neurosci* 12: 88, 2018. doi:10.3389/fnins.2018.00088.

Priesol AJ, Valko Y, Merfeld DM, Lewis RF. Motion perception in patients with idiopathic bilateral vestibular hypofunction. *Otolaryngol Head Neck Surg* 150: 1040–1042, 2014. doi:10.1177/0194599814526557.

Ramos de Miguel A, Falcon Gonzalez JC, Ramos Macias A. Vestibular response to electrical stimulation of the otolith organs. implications in the development of a vestibular implant for the improvement of the sensation of gravitoinertial accelerations. *J Int Adv Otol* 13: 154–161, 2017. doi:10.5152/iao.2017.4216.

Robblee LS, Rose TL. Electrochemical guidelines for selection of protocols and electrode materials for neural stimulation. In: *Neural Prostheses: Fundamental Studies*, edited by Agnew WF, McCreery DB. Englewood Cliffs, NJ: Prentice Hall, 1990, p. 26–66.

Robinson DA. A method of measuring eye movement using a scleral search coil in a magnetic field. *IEEE Trans Biomed Eng* 10: 137–145, 1963. doi:10.1109/tbmel.1963.4322822.

Strupp M, Kim JS, Murofushi T, Straumann D, Jen JC, Rosengren SM, Della Santina CC, Kingma H. Bilateral vestibulopathy: Diagnostic criteria consensus document of the classification committee of the barany society. *J Vestib Res* 27: 177–189, 2017. doi:10.3233/VES-170619.

Sun DQ, Lehar M, Dai C, Swarthout L, Lauer AM, Carey JP, Mitchell DE, Cullen KE, Della Santina CC. Histopathologic changes of the inner ear in rhesus monkeys after intratympanic gentamicin injection and vestibular prosthesis electrode array implantation. *J Assoc Res Otolaryngol* 16: 373–387, 2015. doi:10.1007/s10162-015-0515-y.

Sun DQ, Ward BK, Semenov YR, Carey JP, Della Santina CC. Bilateral vestibular deficiency: quality of life and economic implications. *JAMA Otolaryngol Head Neck Surg* 140: 527–534, 2014. doi:10.1001/jamaoto.2014.490.

Suzuki JI, Tokumasu K, Goto K. Eye movements from single utricular nerve stimulation in the cat. *Acta Otolaryngol* 68: 350–362, 1969. doi:10.3109/00016486909121573.

Tooker A, Tolosa V, Shah KG, Sheth H, Felix S, Delima T, Pannu S. Optimization of multi-layer metal neural probe design. *Proc Annu Int Conf IEEE Eng Med Biol Soc EMBS* 2012: 5995–5998, 2012. doi:10.1109/EMBC.2012.6347360.

Valentin NS, Hageman KN, Dai C, Della Santina CC, Fridman GY. Development of a multichannel vestibular prosthesis prototype by modification of a commercially available cochlear implant. *IEEE Trans Neural Syst Rehabil Eng* 21: 830–839, 2013. doi:10.1109/TNSRE.2013.2259261.

Valko Y, Lewis RF, Priesol AJ, Merfeld DM. Vestibular labyrinth contributions to human whole-body motion discrimination. *J Neurosci* 32: 13537–13542, 2012. doi:10.1523/JNEUROSCI.2157-12.2012.

Wall C 3rd, Kos MI, Guyot JP. Eye movements in response to electric stimulation of the human posterior ampullary nerve. *Ann Otol Rhinol Laryngol* 116: 369–374, 2007. doi:10.1177/000348940711600509.

Ward BK, Agrawal Y, Hoffman HJ, Carey JP, Della Santina CC. Prevalence and impact of bilateral vestibular hypofunction: results from the 2008 US National Health Interview Survey. *JAMA Otolaryngol Head Neck Surg* 139: 803–810, 2013. doi:10.1001/jamaoto.2013.3913.

Whitney SL, Rossi MM. Efficacy of vestibular rehabilitation. *Otolaryngol Clin North Am* 33: 659–672, 2000. doi:10.1016/S0030-6665(05)70232-2.

Yang TH, Liu SH, Wang SJ, Young YH. An animal model of ocular vestibular-evoked myogenic potential in guinea pigs. *Exp Brain Res* 205: 145–152, 2010. doi:10.1007/s00221-010-2346-8.

Yates BJ, Bronstein AM. The effects of vestibular system lesions on autonomic regulation: observations, mechanisms, and clinical implications. *J Vestib Res* 15: 119–129, 2005.

Yates BJ, Miller AD. Properties of sympathetic reflexes elicited by natural vestibular stimulation: implications for cardiovascular control. *J Neurophysiol* 71: 2087–2092, 1994. doi:10.1152/jn.1994.71.6.2087.

Zee DS, Hain TC. Clinical implications of otolith-ocular reflexes. *Am J Otol* 13: 152–157, 1992.

Zhu H, Jordan JR, Hardy SPG, Fulcher B, Childress C, Varner C, Windham B, Jeffcoat B, Rockhold RW, Zhou W. Linear acceleration-evoked cardiovascular responses in awake rats. *J Appl Physiol (1985)* 103: 646–654, 2007. doi:10.1152/japplphysiol.00328.2007.